3D DYNAMIC STALL SIMULATION OF FLOW OVER NACA0012 AIRFOIL AT 10^5 AND 10^6 REYNOLDS NUMBERS

Venkata Ravishankar Kasibhotla

Thesis submitted to the faculty of the Virginia Polytechnic Institute and State University in partial fulfillment of the requirements for the degree of

Master of Science

In

Mechanical Engineering

Danesh K. Tafti, Chair

Francine Battaglia

Mark R. Paul

February 26, 2014

Blacksburg, VA

Keywords: Dynamic Stall, Computational Fluid Dynamics, Large Eddy Simulation, Boundary Fitted Moving Grid, Reduced Frequency

3D Dynamic Stall Simulation of Flow over NACA0012 Airfoil at 10^5 and 10^6 Reynolds Numbers

Venkata Ravishankar Kasibhotla

Abstract

The work presented in this thesis attempts to provide an understanding of the physics behind the dynamic stall process by simulating the flow past pitching NACA-0012 airfoil at 10^5 and 10^6 Reynolds number based on the chord length of the airfoil and at different reduced frequencies of 0.188 and 0.25 respectively in a three dimensional flow field. The mean angles of attack are 12^0 and 15^0 and the amplitudes of pitching are 6^0 and 10^0 respectively. The turbulence in the flow field is resolved using large eddy simulations with dynamic Smagorinsky model at the sub grid scale. The lift hysteresis plots of this simulation for both the configurations are compared with the corresponding experiments. The development of dynamic stall vortex, vortex shedding and reattachment as predicted by the present study are discussed in detail.

There is a fairly good match between the predicted and experimentally measured lift coefficient during the upstroke for both cases. The net lift coefficient for the $Re_c = 10^5$ case during downstroke matches with the corresponding experimental data, the present study under-predicts the lift coefficient as compared to the experimental values at the start of downstroke and over-estimates for the remaining part of the downstroke. The trend of the lift coefficient hysteresis plot with the experimental data for the $Re_c = 10^6$ case is also similar. This present simulations have shown that the downstroke phase of the pitching motion is strongly three dimensional and is highly complex, whereas the flow is practically two dimensional during the upstroke.

Dedicated to my wife Meera

Acknowledgements

This work was made possible by the partial support of Army Research Office under the grant W911NF-08-1-0433. This study was conducted at the High Performance Computational Fluid-Thermal Science and Engineering Lab, headed by Dr. Danesh K Tafti, the William S. Cross Professor at the Department of Mechanical Engineering at Virginia Tech. I thank him for the support and for providing me with the opportunity to expand my knowledge in LES techniques. I also thank my committee members Dr. Francine Battaglia and Dr. Mark Paul for reviewing my research and serving on my committee.

I would like to thank my present and former lab mates (Amit, Deepu, Husam, Kamal, Long, Nagi, Naresh, Sukhi, Surjo, Vivek) for making the lab a fun place for research. I enjoyed all the wonderful technical discussions that we had in the lab.

Last but not the least I would like to extend my thanks to the Advanced Research Computing at Virginia Tech for providing the computational resources and technical support that have contributed to the results reported within this study.

Table of Contents

List of Figures

Nomenclature

α	Angle of Attack (AoA) in degrees
α_m	Mean Angle of Attack (AoA) of the Pitching Cycle
α_{min}	AoA at the Minimum Amplitude of the Pitching Cycle
α_{max}	AoA at the Maximum Amplitude of the Pitching Cycle
A_p	Projected Surface Area of the Airfoil
c	Airfoil Chord Length
C_L	Lift Coefficient
C_p	Pressure Coefficient
C_S	Smagorinsky Constant
ΔS	First Cell Thickness off the Solid Wall
ξ, η, ζ	Jacobians in the x, y and z directions
f	Frequency of Pitching Cycle
k	Reduced Frequency of Pitching Cycle
L	Lift Force on the Airfoil Surface
L^*	Reference Dimensional Length Scale
M	Mach Number of the Flow
ν	Kinematic Viscosity of the Fluid
p	Non-dimensional Static Pressure
ρ	Density of the Fluid
Re_t	Turbulent Reynolds Number
S	Normal Projected Area of the Airfoil
τ_w	Wall Shear Stress
U	Axial Velocity
U_∞	Free Stream Velocity
U^*	Reference Dimensional Velocity Scale
U_{fric}	Frictional Velocity
y^+	Fluctuating Velocity Component
t	Dimensionless Wall Distance
t^*	Reference Dimensional Time Scale
x	X coordinate
y	Y Coordinate
z	Z Coordinate
$\uparrow$	Angle during Upstroke
$\downarrow$	Angle during Downstroke

1. Introduction

Dynamic stall is a term used to describe the complex series of events that result in delay in the stall on airfoils or wings when pitched in a simple harmonic motion about a mean angle of attack (α_m). This nonlinear and unsteady aerodynamic phenomenon appears in helicopter rotors, aircraft wings, and vertical axis wind turbines (VAWTs), turbo-machinery blades and even insect wings[1] and can greatly impact the design parameters such as lift coefficient and pitching moment. Kramer[2] first identified the features associated with the dynamic stall in a rapidly varying incidence angle experienced by an airfoil. The importance of dynamic stall was first emphasized by the helicopter design community in the 1960s when the designers were confused by the extra lift gained on the helicopter rotor in the retreating phase. Although the onset of stall can be delayed by the pitching motion of the airfoil, but once the dynamic stall occurs the vibratory loads caused by the unsteady aerodynamic loads can be unacceptably severe and can considerably reduce the fatigue life of the airfoil. Accurate prediction of dynamic stall phenomenon at high Reynolds numbers is important to ensure efficiency in design of modern aircrafts and helicopters.

To improve the prediction of dynamic stall events of the flow over an airfoil, proper treatment of turbulence within the flow is needed for two important reasons. The first reason is to capture the effect of boundary layer transition which influences the onset of stall and subsequent flow reattachment after the massive flow separation. The second reason is to accurately capture the three dimensional nature of the vortices that get generated and shed during the pitching cycle.

Several experiments have been performed to study the dynamic stall phenomenon which is characterized by the initiation, growth, and convection and shedding of a strong leading edge vortex.[2-10] The flow behavior of dynamic stall strongly depends on Reynolds number, Mach number, mean and amplitude of pitching cycle, reduced frequency of oscillation and shape of the airfoil.[11] The role of boundary layer transition in the simulation of dynamic stall has been the focus of several CFD studies.[12, 13] There are few turbulence models that can predict the boundary layer transition and onset of separation during upstroke of the pitching cycle, where the flow is fully attached for the most part and

two dimensional simulations are sufficient to obtain good agreement with the experimental data. The statistical RANS models are designed and calibrated on the basis of mean parameters of thin turbulent shear layers containing numerous and relatively standard eddies.[14] The flow behavior during downstroke is highly unsteady and is dominated by the separated flow containing comparatively fewer and geometry specific three dimensional vortical structures. Thus it is important to accurately model the small scales near the wall and resolve large scales at the massively separately regions.

Dynamic stall phenomenon, in most of the applications, is highly turbulent due to high Reynolds numbers involved. Progress in the discretization schemes and numerical algorithms for solving the fluid flow problems achieved over the last few years together with the enormous increase in computing capabilities enable detailed computations with highly accurate spatial and temporal resolution and dense meshes. However those numerical simulations will only contribute to a better understanding of dynamic stall mechanisms when the progress in better numerical schemes is coupled with the progress in the improvement of methods for modeling and resolving the turbulent flows. Better modeling of transitional flow regions which play a vital role in the overall flow field development is also important.

Turbulent flows are three-dimensional and include a wide range of space and time scales, which widen with increasing Reynolds number. A detailed computation of all the scales existing in turbulence (DNS) from the large scale eddies down to the Kolmogorov scales which are fully described by the Navier-Stokes equations without additional external information, imposes enormous requirements in computing speed and storage capacity. DNS is not expected to play a role for the investigation of dynamic stall due to the enormous computing resources they require and because they are limited to simple flow geometries. Numerical investigation of practical flows requires the modeling of small eddy motions that cannot be resolved in space and time, and therefore require some kind of turbulence modeling. There are two types of turbulence models applied to the solution of practical aerodynamic flow problems, sub-grid modeling in the full Navier-Stokes simulations and statistical turbulence modeling in the Reynolds averaged Navier-Stokes equations.

The scale selection that the large eddy simulation technique is based on is a separation between large and small scales. In order to define these two categories, first a reference or cutoff length has to be determined. Those scales that are of characteristic size greater than the cutoff length are known as large or resolved scales while others are called small or sub-grid scales.[15] LES simulations resolve large scales in both space and time, and the behavior of small unresolved scales is described by the sub-grid model. The computational requirements for LES even for simple, steady airfoil flows are very high. However, LES has the potential in improving dynamic stall calculations because they resolve the large eddies which are unique for this type of flow condition (direction and geometry dependent) and model the smaller scales of turbulence that are isotropic.

The accuracy of the simulations for predicting dynamic stall is highly dependent on the turbulence model that is used. Several authors used eddy viscosity based turbulence models for simulating the dynamic stall phenomenon, such as Baldwin-Lomax, Spalart-Allmaras, standard $k-\epsilon$, RNG $k-\epsilon$, baseline $k-\omega$.[16-34] The previous studies concluded that one equation turbulence models provide significant improvement over the algebraic and half equation models. Most of the two equation turbulence models failed to match with the experimental data especially at high angles of attack and at high reduced frequencies. Another set of 2D dynamic stall computations of NACA0012 airfoil at 10^5 Reynolds number were done with two sets of pitching patterns, different reduced frequencies, mean oscillating angles and amplitudes with turbulence treatment done using URANS.[35] Two URANS models, namely the standard $k-\omega$ model and the SST $k-\omega$ model with transition modeling were used. The study concluded that the standard $k-\omega$ model is too dissipative to predict the severe adverse pressure gradient on the suction surface of the airfoil. The SST $k-\omega$ model shows improvement over the standard $k-\omega$ model, but fails to match with the experimental data at high angles of attack where the three dimensional effects are expected to be more dominant.

1.1 Literature Review

During the past three decades, dynamic stall phenomenon has received great deal of attention from researchers all around the world. There are numerous research studies (both experimental and numerical) that have focused on the physics leading to dynamic stall and the factors such as Reynolds number, Mach number, pitch rate (reduced frequency) and amplitude affecting this complex phenomenon. Reduced frequency is a dimensionless number used in general for the case of unsteady aerodynamics and aeroelasticity.[36] It is one of the parameters that defines the degree of unsteadiness of the problem. Reduced frequency can be used to explain the amplitude attenuation and the phase lag of the unsteady aerodynamic forces compared to the quasi steady analysis (which in theory assumes no phase lag). Reduced frequency (k) is defined as: $k = {(\pi f c)}/{U_\infty}$

where f = Oscillation frequency, c = Airfoil Chord Length and U_∞ = Free stream velocity. Based on the value of the reduced frequency (k), we can roughly divide the flow into:

- Steady state aerodynamics where $k = 0$
- Quasi-steady aerodynamics where $0 \leq k \leq 0.05$
- Unsteady aerodynamics where $k > 0.05$ ($k > 0.2$ is considered highly unsteady)

The unsteady flow separation phenomenon on pitching airfoils is not yet completely understood at high Reynolds numbers.

For dynamic stall occurring at $\mathrm{M}_\infty \leq 0.2$, compressibility effects are negligible even at the airfoil leading edge where the flow accelerates as the angle of attack increases. Mehta[26] computed the laminar incompressible flow past an oscillating NACA0012 airfoil at Reynolds numbers of 5×10^3 and 10^4 to gain insight into the mechanism of dynamic stall using vorticity-stream function approach. The oscillatory motion was given by $\alpha(t) = [1 - \cos(\omega t)]$ with reduced frequencies of $k = 0.25$ and 0.50. Good qualitative agreement of computation with water tunnel flow visualization was obtained. This was first of the numerical simulation of dynamic stall at moderately high Reynolds numbers.

Ghia et al.[27] have also investigated laminar incompressible dynamic stall flow fields using vorticity-stream function formulation for flow over NACA0015 airfoil at Reynolds numbers of 10^4 and 45×10^3. The oscillatory motion was given by $\alpha(t) = k\left[t - \left({}^{t_0}/_{4.6}\right)\left(1 - e^{-\left({}^{4.6}/_{t_0}\right)t}\right)\right]$ with reduced frequency of $k = 0.2$. In the same study, the effect of leading edge suction and the trailing edge injection in controlling the dynamic stall was also investigated. Favorable comparison of the computation with the smoke flow visualization was obtained. Lift hysteresis curve is also closely matched with the experimental values from the pressure taps.

Laminar and turbulent incompressible dynamic stall flow fields were investigated numerically by Wu et al.[16, 28], using velocity-vorticity formulation. Fully turbulent solutions were obtained at $Re = 10^6$ for sinusoidal oscillation of a NACA0012 airfoil with $\alpha(t) = 15^0 + 10^0 \sin(\omega t)$ at different reduced frequencies of $k = 0.1, 0.15$ and 0.25 as shown in the Figure 1.1.[28] The Baldwin-Lomax turbulence model was used for the prediction of the turbulent flow behavior. The analysis concluded that the formation of the leading edge vortex is delayed to higher angles of attack as the reduced frequency of pitching motion is increased. All the results from this study showed consistent under prediction of the lift coefficient both during the upstroke as well as during the downstroke. However the overall trend of the lift hysteresis plot matched with that of the experiments.

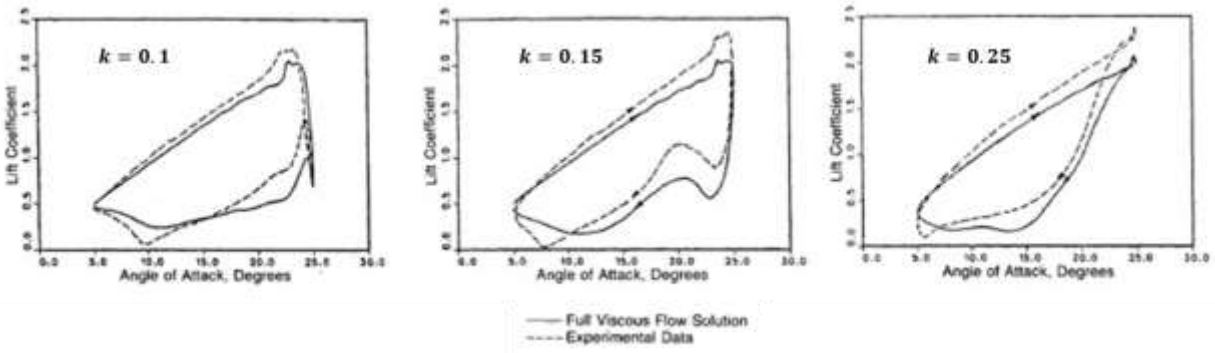

Figure 1.1: Lift Hysteresis Comparison Plots. Reprinted from Tuncer, I., Wu, J., Wang, C., 1990, "Theoretical and Numerical Studies of Oscillating Airfoils," AIAA Journal, 28(9), pp. 1615-1624. Used with Permission of AIAA, 2014

$$\boldsymbol{\alpha(t) = 15 + 10\sin(\omega t)\,, Re_c = 1 \times 10^6}$$

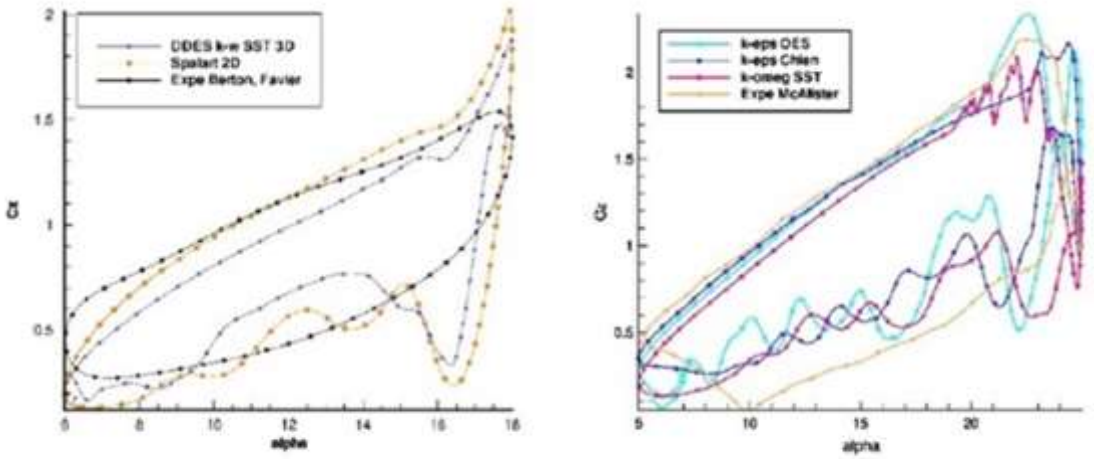

$Re_c = 10^5; k = 0.188$ $Re_c = 10^6; k = 0.1$

Figure 1.2: Lift Hysteresis Comparison Plots. Reprinted from Martinat, G., Braza, M., Hoarau, Y., Harran, G., 2008, "Turbulence Modeling of the Flow Past a Pitching NACA0012 airfoil at 10^5 and 10^6 Reynolds Numbers," Journal of Fluids and Structures, 24, pp. 1294-1303. Used with Permission of Elsevier, 2014.

$$\boldsymbol{\alpha(t) = 12 + 6\sin(\omega t), k = 0.188 \text{ and } \alpha(t) = 15 + 10\sin(\omega t), k = 0.1}$$

2D and 3D dynamic stall simulations were performed on NACA0012 airfoil at Reynolds numbers of 10^5 and 10^6 at reduced frequencies of $k = 0.188$ and 0.1 respectively as shown in the Figure 1.2.[37] The pitching motion was given by $\alpha(t) = 12 + 6\sin(\omega t)$ for $Re_c = 10^5$ case and $\alpha(t) = 15 + 10\sin(\omega t)$ for $Re_c = 10^6$ case. The spatial discretization is done using third order upwind (Roe) with MUSCL flux evaluation and the temporal scheme is second order in accuracy. The turbulence effect of dynamic stall is included using URANS with Organized Eddy Simulation and this turbulence modeling has shown quite dissipative character that attenuates the instabilities and vortex structures related to dynamic stall. The lift hysteresis plot shows that there is more than 50% error in predicting the lift coefficient at the start of downstroke for $Re_c = 10^5$ case and the predicted lift coefficient is offset by 0.3 for the most of the downstroke for $Re_c = 10^6$ case.

Compressible, unsteady, turbulent flow computations were obtained by Sankar and Tang[31] and Rumsey and Anderson[33]. The latter investigators computed dynamic stall at transonic speeds and the

numerical simulations are in agreement with the experiments. Dynamic stall of a SSC-A09 Sikrosky airfoil executing rapidly pitching motions was investigated by Ekaterinaris[34] for turbulent $\mathrm{Re_c} = 2 \times 10^6$. An implicit finite-difference scheme was used for the numerical solution of the compressible form of Navier-Stokes equations and the turbulence closure was done using Baldwin-Lomax algebraic model.

Numerical investigations of dynamic stall at high Reynolds numbers conducted by Fung and Carr[38] concluded that an increase in reduced frequency delays boundary layer separation and allows the airfoil to attain higher lift values at higher angles of attack. In more recent work, Currier and Fung[39] concluded that airfoil shape is also an important factor in addition to reduced frequency in determining the size and shape of lift hysteresis.

A conclusion of the early numerical investigations of dynamic stall in turbulent high Reynolds number flows was that the overall prediction of lift hysteresis using algebraic turbulence models was in good agreement with the experimental data. But they cannot accurately simulate the massively separated flow at high angles of incidence, especially during downstroke. However, even with the two equation RANS turbulence closure, the lift coefficient during the start of downstroke did not show improvement as compared to the Baldwin-Lomax algebraic turbulence model.[16] The more recent study on the simulation of the onset of dynamic stall using high fidelity Implicit Large Eddy Simulations (ILES) was performed by Visbal[40] concluded that for moderately high Reynolds numbers (typically less than 1 million) the laminar separation bubble (LSB) plays a critical role in the propagation of transition along the pitching airfoil and the quantitative prediction of the collapse of suction and dynamic stall vortex.

1.2 Research Objectives

It is generally accepted that wall resolved large eddy simulation (LES) is a promising tool for highly unsteady turbulent flows which are dominated by the boundary layer transition, shear instabilities, large separation and recirculation regions, vortex formation and shedding. With the advent of high speed computers and parallel processing, LES can be used to understand the dynamic stall physics of relatively high Reynolds number flows. To the best of the author's knowledge there are very few previous studies

on using wall resolved LES for dynamic stall simulation at high Reynolds numbers.[40, 41] Therefore the objective of the present study is to assess the ability of Large Eddy Simulation to accurately simulate the flow over an oscillating NACA0012 airfoil at $Re_c = 10^5$ $Re_c = 10^6$ at different reduced frequencies in order to make a contribution towards a better understanding of the flow physics of dynamic stall.

2. Computational Methodology

This chapter discusses in detail, the numerical methodology used for the present study along with the computational set up which includes the computational grid details and the applied boundary conditions. The first section discusses the governing equations relevant to simulation of dynamic stall. There is a section that discusses the grid movement algorithm and its implementation in the current solver framework. There is also a separate section on the turbulence treatment in the present study.

The process of CFD simulation begins with the creation of a three dimensional domain and its proper discretization. The section on grid generation discusses the philosophy of cell distribution and sizing adopted for this study. The last section of this chapter deals with the application of boundary conditions to the computational domain for the simulation.

2.1 Governing Equations

The governing equations for the time-dependent, incompressible viscous flow in a moving frame of reference consist of space, mass and momentum conservation laws. The equations are mapped from physical $(\vec{x})$ to computational space $(\vec{\xi})$ by a boundary conforming transformation $\vec{x} = \vec{x}(\vec{\xi})$, where $\vec{x} = (x, y, z)$ and $\vec{\xi} = (\xi, \eta, \zeta)$. The equations are non-dimensionalized by a suitable length (c) and velocity scale (U_∞) and written in conservative non-dimensional form as:

Space Conservation (SCL):

$$\frac{\partial}{\partial t}\left(\sqrt{g}\right) - \frac{\partial}{\partial \xi_j}\left(\sqrt{g}U_g^j\right) = 0 \tag{2.1}$$

Mass Conservation:

$$\frac{\partial}{\partial \xi_j}\left(\sqrt{g}U^j\right) = 0 \tag{2.2}$$

Momentum Conservation:

$$\frac{\partial}{\partial t}\left(\sqrt{g}u_i\right)+\frac{\partial}{\partial \xi_j}\left(\left[\sqrt{g}U^j-\sqrt{g}U_g^j\right]u_i\right)=-\frac{\partial}{\partial \xi_j}\left(\sqrt{g}\left(\vec{a}^j\right)_i p\right)+\frac{\partial}{\partial \xi_j}\left(\left[\frac{1}{Re}+\frac{1}{Re_t}\right]\sqrt{g}g^{jk}\frac{\partial u_i}{\partial \xi_k}\right) \quad \textbf{(2.3)}$$

where $\sqrt{g}$ is the Jacobian of the transformation, $\vec{a}^i$ are the contra-variant basis vectors, $\sqrt{g}U^j=\sqrt{g}\left(\vec{a}^j\right)_k u_k$ is the contra-variant flux vector, $\sqrt{g}U_g^j=\sqrt{g}\left(\vec{a}^j\right)_k u_k^g$ is the contra-variant flux vector due to the grid velocity u^g, g^{ij} is the contravariant metric tensor, u_i is the Cartesian velocity vector, and P is the pressure. In the above formulation, the grid velocity u^g is not used explicitly. Instead, the grid contra-variant flux vector is employed which is directly computed based on the SCL. The time is non-dimensionalized using $\left(t^* U_\infty/c\right)$ and the Reynolds number is given by $\left(U_\infty c/\nu\right)$.

2.2 Turbulence Treatment

Re_t is the inverse of the subgrid eddy-viscosity which is modeled as:

$$\frac{1}{Re_t}=C_s^2\left(\sqrt{g}\right)^{2/3}\left|\overline{S}\right| \quad \textbf{(2.4)}$$

$\left|\overline{S}\right|$ is the magnitude of the strain rate tensor given by $\left|\overline{S}\right|=\sqrt{2\overline{S_{ij}}\,\overline{S_{ij}}}$ where $\overline{S_{ij}}$ is the strain rate of the resolved flow field and the Smagorinsky constant C_s^2 is obtained via the dynamic sub-grid stress model (Germano et al.[42]). To this end, a second test filter, denoted by $\hat{G}$, is applied to the filtered governing equations with the characteristic length scale of $\hat{G}$ being larger than that of the grid filter $\overline{G}$. The test filtered quantity is obtained from the grid filtered quantity by a second-order trapezoidal filter which is given by $\hat{\phi}=\frac{1}{4}\left(\overline{\phi_{i-1}}+2\overline{\phi_i}+\overline{\phi_{i+1}}\right)$ in one dimension. The resolved turbulent stresses, representing the energy scales between the test and grid filters, $L_{ij}=\widehat{\overline{u_i}\overline{u_j}}-\hat{\overline{u}}_i\hat{\overline{u}}_j$, are then related to the subtest, $T_{ij}=\widehat{\overline{u_i}\overline{u_j}}-\hat{\overline{u}}_i\hat{\overline{u}}_j$, and subgrid-scales stresses $\tau_{ij}=\overline{u_iu_j}-\overline{u}_i\overline{u}_j$ though the identity, $L_{ij}^a=T_{ij}^a-\hat{\tau}_{ij}^a$.

The anisotropic subgrid and subtest-scale stresses are then formulated in terms of the Smagorinsky eddy viscosity model as:

$$\widehat{\tau_{ij}^{a}} = -2C_s^2(\sqrt{g})^{2/3}\widehat{|\bar{S}|\bar{S}_{ij}}$$

$$T_{ij}^{a} = -2C_s^2\alpha(\sqrt{g})^{2/3}\left|\hat{\bar{S}}\right|\widehat{\bar{S}_{ij}} \quad \textbf{(2.5)}$$

Using the identity

$$\widehat{L_{ij}^{a}} = \widehat{L_{ij}} - \frac{1}{3}\delta_{ij}L_{kk} - 2C_s^2\left(\sqrt{g}\right)^{2/3}\left[\alpha\left|\hat{\bar{S}}\right|\widehat{\bar{S}_{ij}} - \widehat{|\bar{S}|\bar{S}_{ij}}\right] = -2C_s^2\left(\sqrt{g}\right)^{2/3}M_{ij}$$

Here α is the square of the ratio of the characteristic length scale associated with the test filter to that of grid filter and is taken to be $\left[\widehat{\Delta_i}/\Delta_i = \sqrt{6}\right]$ for a representative one-dimensional test filtering operation.

Using a least-squares minimization procedure of Lilly, a final expression for C_s^2 is obtained as:

$$C_s^2 = -\frac{1}{2}\frac{1}{\left(\sqrt{g}\right)^{2/3}}\frac{L_{ij}^{a}\otimes M_{ij}}{M_{ij}\otimes M_{ij}} \quad \textbf{(2.6)}$$

The value of C_s^2 is constrained to be positive by setting it to zero when $C_s^2 < 0$.

2.3 Moving Grid Algorithm

This time dependent grid movement subroutine employs a multi-block framework which facilitates parallelization. The computational domain is divided into non-overlapping contiguous blocks, which are then distributed to multiple processors, the maximum number of which are limited by the total number of blocks. Each block has a separate data structure and the Message Passing Interface (MPI) is used for data transfer across processors. Further, within each block, virtual cache blocks are used while solving linear systems. A detailed description of the software architecture can be found in Tafti[43]. The algorithm

decouples the grid movement from the application of fluid conservation laws. The steps involved in the calculation of unsteady flow in the dynamic grid system can be summarized as follows:

1. The initial grid is read and the values of dependent variables are initialized.
2. The nodes on moving boundaries are displaced based on a prescribed or induced motion and velocity boundary conditions are computed based on the displacement.
3. The boundary movement is then transmitted to the interior of the domain in the rezoning phase. The transmittal of boundary motion to volume grid motion is done in a hierarchy of steps.
    a. First the corner displacements of each computational block are computed using the spring analogy.
    b. Second, the corner displacement of each block is transmitted to the nodal distribution in block edges, block faces, and block volumes, respectively, by using a modified TFI procedure. This step completes the rezoning phase.

    It is noted that rezoning is only implemented when the mesh deforms. If instead the boundary movement is uniformly transmitted into the domain as in a certain class of problems, the rezoning step is not necessary.
4. New grid metrics and the contra-variant flux due to grid movement are computed by satisfying the SCL condition (Eqn. 2.1).
5. The mass and momentum equations given by Eqns. (2.2-2.3) are advanced in time using a fractional-step algorithm to complete the time step.

At the next time advancement, steps 2 to 5 are repeated. The detailed flow chart of the aforementioned process is shown in the Figure 2.1.

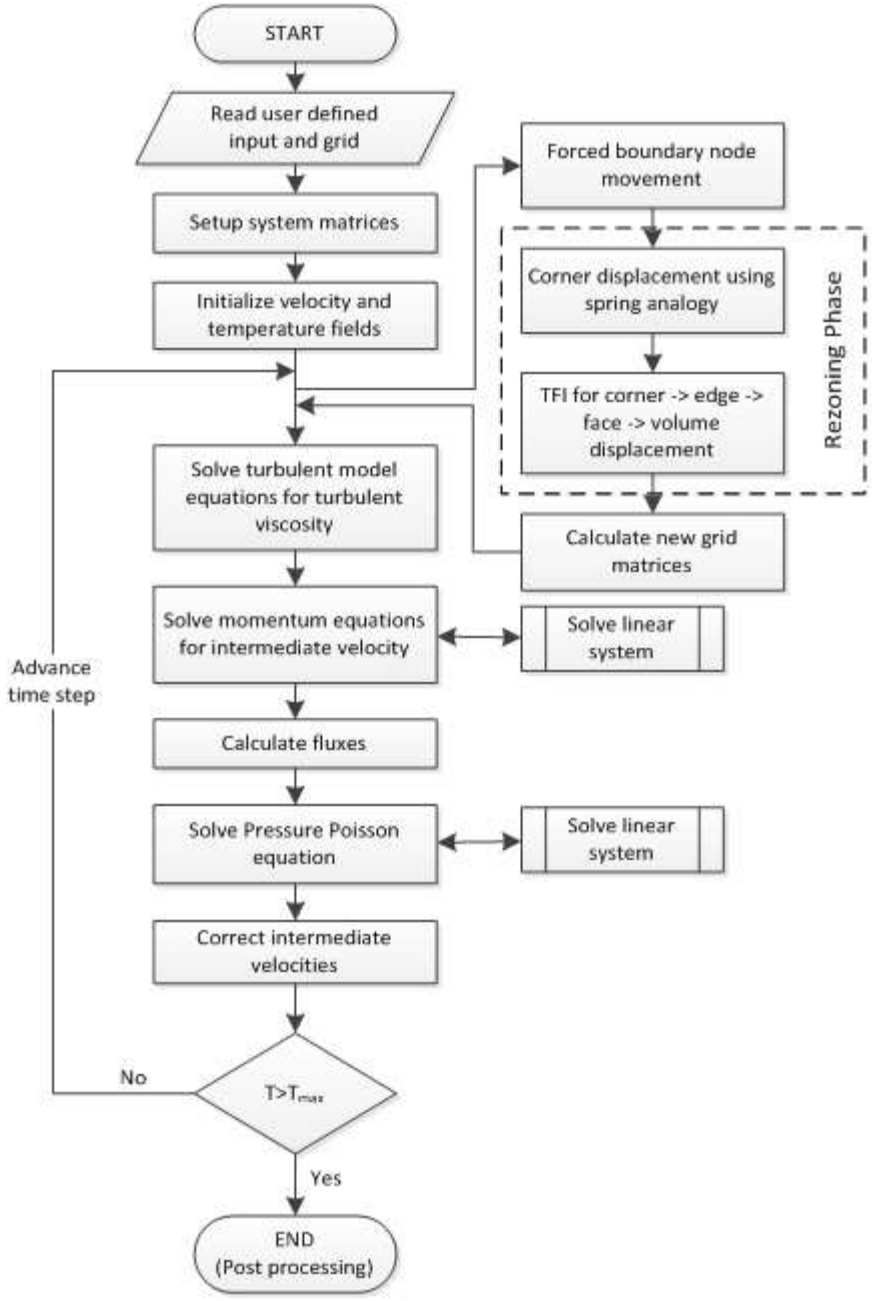

Figure 2.1: GenIDLEST Solver Flowchart

2.3.1 Rezoning Phase

The rezoning is done at the start of the time step to adjust the grid based on boundary movement. The location of the moving boundary at a new time is evaluated based on the prescribed or induced motion. The velocity of the moving boundary is then computed as $\vec{u}_b = {d\vec{x}}/{dt}$ and applied as a boundary

condition. The rezoning is carried out in two steps. In the first step the movement of each block corner is computed by using a spring analogy similar to that of Tsai[44]. In the parallel architecture, since blocks are located on different processors, the evaluation of block corner displacements is carried out on a master processor. The displacement of the internal corner is evaluated based on the movement of the external corners, which are located either on a moving or a fixed boundary. Then the displacement of block corners is broadcast to all processors. In the second step the modified TFI[44-46] based on corner displacements are carried out for each block. The main advantage of the modified TFI is that it can be carried out in parallel and by using the same interpolation technique across processors. The same grid distribution is obtained at block interfaces residing on different processors, hence eliminating any extra communication between processors. Further, since the TFI is applied only on displacement. i.e. the displaced grid is obtained by adding interpolated displacements to the old grid locations, the quality of the initial grid is maintained for simple boundary movements. Further details of the boundary fitted finite-volume moving grid technique based on Arbitrary Lagrangian Eulerian (ALE) method and its implementation in GenIDLEST solver is provided in one of the references.[47]

2.4 Numerical Algorithm

After evaluating the new grid metrics and the grid contra-variant fluxes, the integration of the Navier-Stokes equations is carried out. The governing Eqn. 2.2-2.3 are discretized with a conservative finite-volume formulation on a non-staggered grid topology. The Cartesian velocities and pressure are calculated and stored at the cell center, whereas contra-variant fluxes are stored and calculated at the cell faces. The temporal advancement is performed in two steps, a predictor step, which calculates an intermediate velocity field, and a corrector step, which calculates the updated velocity at the new time step by satisfying discrete continuity.[43]

2.4.1 Predictor Step

$$\frac{\sqrt{g}^{n+1}\tilde{u}_i - \sqrt{g}^{n}u_i^n}{\Delta t} = D_i - C_i \tag{2.7}$$

where D_i is the diffusion term and C_i is convection due to flow and grid movement. In this study, convection and diffusion terms are treated implicitly by a Crank-Nicolson scheme.

Convection Terms:

$$C_i = \frac{\partial}{\partial \xi_j}\left(\sqrt{g}U^j u_i\right)^{n+1/2} - \frac{\partial}{\partial \xi_j}\left(\sqrt{g}U_g^j u_i\right)^{n+1/2} \tag{2.8}$$

The values of grid contra-variant fluxes, available at time level $n + {}^1/_2$ from SCL condition are used in the momentum equation.

$$C_i = \frac{1}{2}\left[\frac{\partial}{\partial \xi_j}\left(\sqrt{g}U^j u_i\right)^n + \frac{\partial}{\partial \xi_j}\left(\sqrt{g}\left(U^j\right)^{n+1}\tilde{u}_i\right) - \frac{\partial}{\partial \xi_j}\left(\sqrt{g}\left(U_g^j\right)^{n+1/2}u_i^n\right) - \frac{\partial}{\partial \xi_j}\left(\sqrt{g}\left(U_g^j\right)^{n+1/2}\tilde{u}_i\right)\right] \tag{2.9}$$

The contra-variant fluxes of at time level $n+1$ is linearized using a two-step (n and $n-1$ time level) second order extrapolation as:

$$\sqrt{g}\left(U^j\right)^{n+1} = 2\sqrt{g}\left(U^j\right)^n - \sqrt{g}\left(U^j\right)^{n-1} \tag{2.10}$$

Diffusion Terms:

$$D_i = \frac{1}{2}\left[\frac{\partial}{\partial \xi_j}\left[\left(\frac{1}{Re} + \frac{1}{Re_t}\right)\sqrt{g}g^{jk}\frac{\partial u_i^n}{\partial \xi_k}\right] + \frac{\partial}{\partial \xi_j}\left[\left(\frac{1}{Re} + \frac{1}{Re_t}\right)\sqrt{g}g^{jk}\frac{\partial \tilde{u}_i}{\partial \xi_k}\right]\right] \tag{2.11}$$

2.4.2 Corrector Step

In this step, the continuity equation is used to derive the pressure equation, which is solved to obtain the pressure field at time level $(n+1)$. The procedure used in formulating the pressure equation is represented as follows:

First the intermediate cell face contra-variant fluxes are constructed as follows:

$$\sqrt{g}\tilde{U}^j = \sqrt{g}\left(\vec{a}^j\right)_i \tilde{u}_i \tag{2.12}$$

Then, the correction form of the cell centered Cartesian velocities and cell face contra-variant fluxes are written as:

$$u_i^{n+1} = \tilde{u}_i - \Delta t\left(\vec{a}^j\right)_i \frac{\partial p^{n+1}}{\partial \xi_j} \tag{2.13}$$

$$\sqrt{g}\left(U^i\right)^{n+1} = \sqrt{g}\tilde{U}^i - \Delta t\sqrt{g}g^{ik}\frac{\partial p^{n+1}}{\partial \xi_k} \tag{2.14}$$

Finally, Eqn. 2.14, in conjunction with Eqn. 2.2, is used to derive the pressure equation, which takes the form:

$$\frac{\partial}{\partial \xi_j}\left(\sqrt{g}g^{jk}\frac{\partial p^{n+1}}{\partial \xi_k}\right) = \frac{1}{\Delta t}\left(\frac{\partial \sqrt{g}\tilde{U}^j}{\partial \xi_j}\right) \tag{2.15}$$

By using the contra-variant fluxes at the cell faces in constructing the pressure equation, the method emulates a staggered grid arrangement. The pressure field at level $n+1$ is then used to correct the nodal Cartesian velocities and the cell face contra-variant fluxes using Eqn. (2.13) and Eq. (2.14) respectively.

2.5 Computational Grid

The computational grid used in the present study is a 'C' topology block-structured grid with the number of blocks being 300 and approximately 45 million control volumes in total. This large mesh size was inevitable in order to satisfy the structured grid topology in the current domain extent along with maintaining the aspect ratio requirements. The present solver GenIDLEST is parallelized by domain decomposition with explicit message passing based on MPI. The extent of the domain upstream of the

airfoil is 15c and 60c in the downstream direction. The domain extent used in the span-wise direction is 0.18c which is sufficient to capture the vortex structures in the flow field according to a similar study[48].

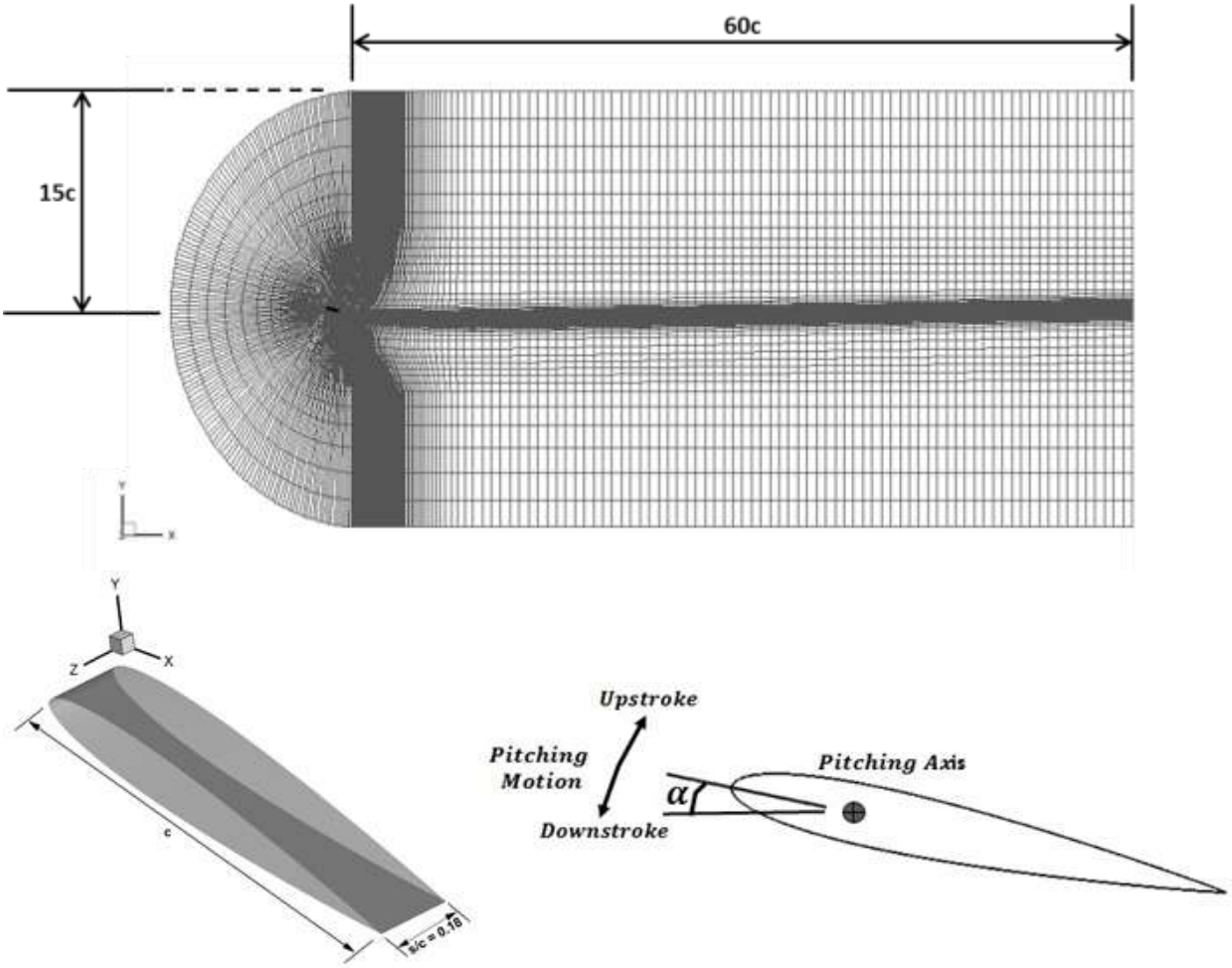

Figure 2.2: Pitching Airfoil Configuration & Sectional Mesh (Every Twelfth grid line is shown)

The x-y plane of the full domain extent of the present simulation is shown in Figure 2.2. The maximum aspect ratio in the computational domain is ~ 50 in the far field and the maximum skewness is ~ 0.45 for the grid at the mean angle of attack condition.

In order to improve the mesh quality near the trailing edge of the airfoil during pitching motion, the block boundaries downstream of the airfoil are given the shape of an inverse exponential curve as shown in the Figure 2.3. The internal grid points are then morphed as per the trans-finite interpolation. This

ensures that the mesh skewness is less than 0.5 even during the maximum amplitude condition of the pitching motion.

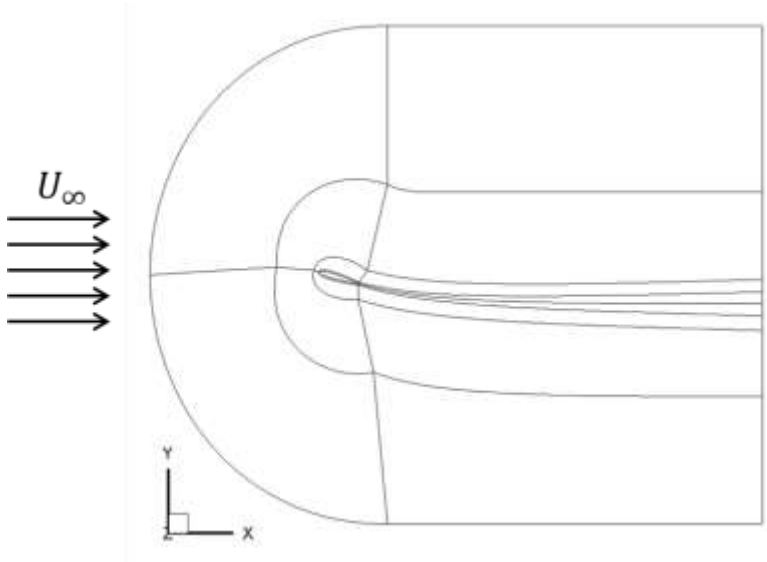

Figure 2.3: Topology of the Inner Blocks of the Computational Domain

The grid points are clustered in the vicinity of the airfoil and at the leading and trailing edges of the airfoil. The height of the first layer of the control volumes is about $\Delta S/c = 4.5 \times 10^{-5}$ and this corresponds to a dimensionless wall distance of $y^+ \approx 0.2$ for the $Re_c = 10^5$ case and $y^+ \approx 1$ for the $Re_c = 10^6$ case at the leading edge of the airfoil at the minimum angle of attack where the mesh requirement for resolving the boundary layer is stringent as compared to other locations. Mesh independency study has not been performed owing to the high computational time requirements.

The present domain extent is chosen in order to ensure that the vortices shed from the airfoil at an angle to the free stream flow direction do not interact with the boundaries. It was observed that when the vortices from the airfoil interacted with the boundary, the solution was prone to numerical instabilities resulting in divergence. Thus a large domain size was chosen. This coupled with the block-structured nature of the grid, the necessity to maintain the grid aspect ratio within 150, and the stringent y^+ requirements of the wall resolved LES, resulted in the grid size of approximately 45 million.

The 300 block geometry was run on 300 processors of Intel Xeon E5-2670 (Sandy Bridge) at Virginia Tech. The run time for 188,000 time steps was approximately 50.4 days with the wall clock time/time step being 23.152 s.

2.6 Boundary Conditions

The present study uses large eddy simulations to resolve the turbulence with dynamic Smagorinsky turbulence model at the sub-grid scales. Free stream velocity is specified at all the external boundaries. Periodic boundary conditions are applied to the span-wise boundary faces along the width of the airfoil. No slip and no penetration boundary conditions are applied to the airfoil surface.

2.7 Lift Coefficient

The lift coefficient (C_L) is a dimensionless number that represents the ratio of the lift force produced by the airfoil to the dynamic pressure force. It is a function of angle of attack (α) of flow relative to the airfoil, Reynoldsnumber (Re), Mach number (Ma) of the flow and shape of the airfoil and is defined as:

$$C_L = \frac{L}{\frac{1}{2}\rho U_\infty^2 S} \tag{2.16}$$

where L is the lift force of the airfoil which is calculated from the following formula:

$$L = \iint \left(p\,\xi_y + \tau_{w,\xi}\,\xi_y + \tau_{w,\eta}\,\eta_y + \tau_{w,\zeta}\,\zeta_y\right) dA_s \tag{2.17}$$

dA_s = Elemental surface area of the airfoil and S = Projected airfoil area normal to the free-stream direction.

The contribution of the first term due to pressure is in general orders of magnitude higher than the magnitude of the contributions due to wall shear stress to the magnitude of the lift coefficient.

2.8 Pressure Coefficient

The pressure coefficient (C_p) is a dimensionless number that describes the relative pressure in the flow field and the closed area of the pressure coefficient over the surface of the airfoil typically represents the magnitude of the lift coefficient.

$$C_p = \frac{p - p_\infty}{\frac{1}{2}\rho U_\infty^2} \tag{2.18}$$

In the flow field where the vortices are present, the location of the vortex center can be identified by the presence of lower pressure surrounded with gradually increasing pressure following the shape of the vortex. It can be noticed that the vortices with higher strength have lower pressure at their core and vice-versa. The next two chapters discuss the change in the lift and pressure coefficient of the flow at different angles of attack during the dynamic stall phenomenon along with the interaction between the vorticity and the pressure at two different Reynolds numbers.

3. Dynamic Stall Simulation of Re = 10^5 case

This chapter discusses in detail about the dynamic stall simulation of flow over NACA0012 airfoil at 10^5 Reynolds number and at reduced frequency of $k = 0.188$. The first section of this chapter provides the details of the experimental setup to which results from the present simulation are compared. The next section provides the simulation details and subsequently the simulation results are discussed. The last two sections provide the comparison of the simulation results with the experimental data and conclusions from the present study.

3.1 Experimental Setup

The experimental test case that is used for validation of the present computational results was done by Berton et al.[49] Experiments were conducted in the high subsonic wind tunnel test section consisting of an octagonal cross section of inside circle of 3 m. in diameter and 6 m. in length. The test section was capable to testing flows with the range of Reynolds number per meter between 3×10^5 and 6×10^6. The airfoil was pitched in a sinusoidal motion about the quarter of the airfoil chord at the same operating conditions as that of the present simulation. The NACA-0012 airfoil cross section was used and the dimensions of the airfoil were 0.48 m. $\times$ 0.956 m. in the chord-wise and span-wise directions respectively. The rectangular airfoil (in the span-wise direction) was mounted vertically between the end plates spanning the test section. The flow velocity field close to the surface of the airfoil surface was measured by the Embedded Laser Doppler Velocimetry (ELDV) technique.

The airfoil was equipped with unsteady pressure transducers mounted flush with the airfoil surface. The static pressure measurements were performed at 16 locations on both the upper and lower side of the airfoil along the chord-wise stations. Both the steady and unsteady pressure distributions had been measured on each side of the wing surface at the mid-span location. Unsteady mean pressure coefficients over the period had been recorded and averaged over 20 consecutive cycles.

3.2 Simulation Details

The equations are solved in a finite volume framework on a block structured, boundary fitted and non-staggered grid using a fractional step algorithm for time advancement. Second order central differences are used for spatial discretization of convective and viscous terms and implicit Crank-Nicolson scheme is used for advancement in time. In past studies at moderate Reynolds numbers, the second-order scheme has been shown to be suitable for LES[50].

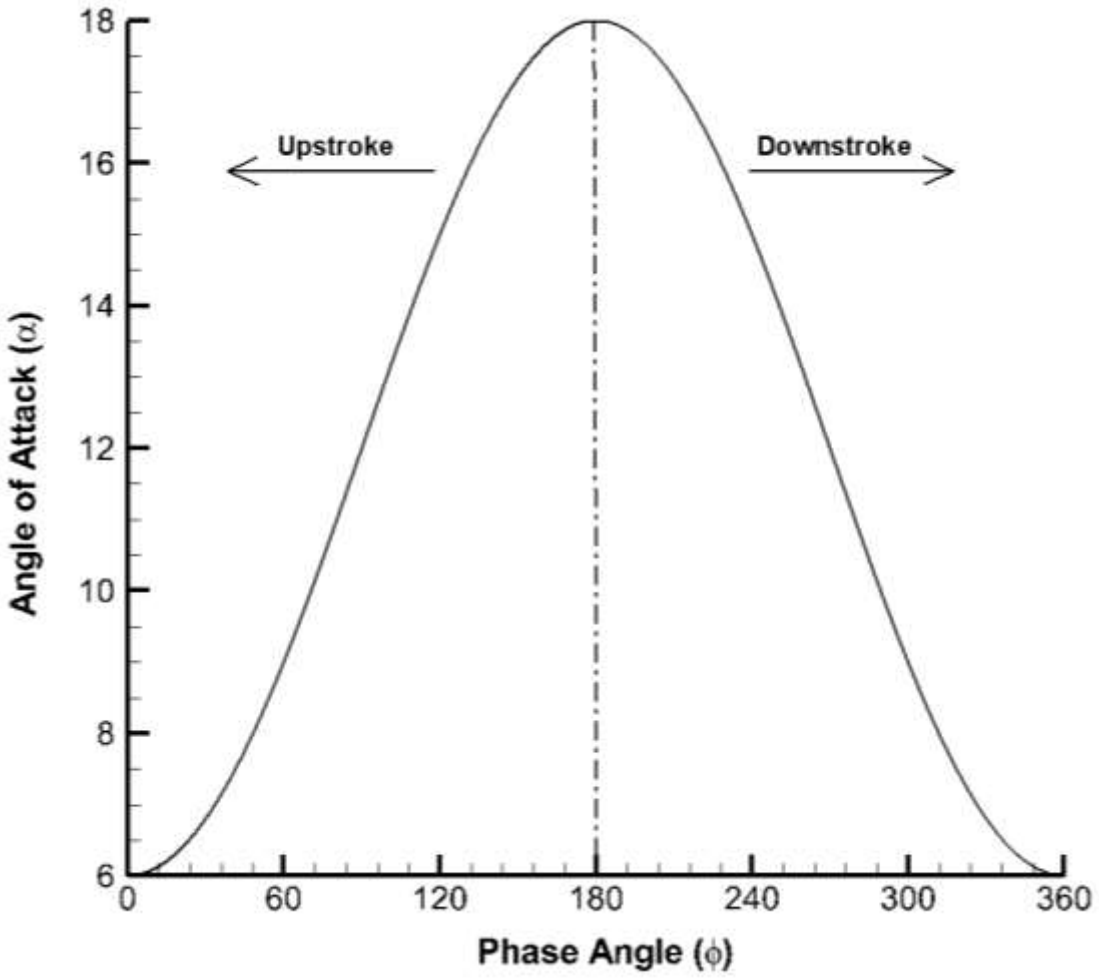

Figure 3.1: Input Angle of Attack Wave Form with Phase Angle for Re = 10^5 case

The forced unsteadiness is generated on the airfoil by means of pitching motion around the quarter chord axis and is defined by the time-dependent angle of attack (α), as shown in the Figure 3.1 is given as:

$$\alpha = \alpha_{\min} + \frac{1}{2}(\alpha_{\max} - \alpha_{\min})(1 - \cos 2kt) \quad \textbf{(3.1)}$$

For this simulation, the angle at the minimum amplitude is $\alpha_{\min} = 6^0$ and the angle at the maximum amplitude is $\alpha_{\max} = 18^0$ oscillating about the mean angle of attack $\alpha_m = 12^0$ $(i.e.\ 12^0 \pm 6^0)$. The reduced frequency of the pitching motion (k) is taken as 0.188.

The initial transient field is generated at the minimum angle of attack $(i.e.\ \alpha_{min} = 6^0)$ by simulating the flow over static airfoil at α_{min} for 8 flow through time units over the length of the airfoil. The oscillatory motion is then introduced and the unsteady flow field is computed by marching in time. The dynamic stall results are reported after simulating for more than two pitching cycles and repeatability in results are observed.

3.3 Results

The development of the unsteady flow field is shown in the instantaneous plots from Figure 3.3 through Figure 3.13. The area enclosed by the pressure coefficient plot represents the lift force acting on the airfoil. During the upstroke (↑), the flow remains attached to the surface of the airfoil from $\alpha \approx 7.2^0$ till $\alpha \approx 12^0$ as shown in the Figure 3.3 and Figure 3.4. During this part of the pitching cycle, lift coefficient varies linearly with the angle of attack (See Figure 3.14). A small and weak recirculating zone is formed near 30% of the chord at $\alpha \approx 7.5^0(\uparrow)$ (See Figure 3.2) during flow reattachment process. This shallow reversed flow region travels upstream and at around $\alpha \approx 12^0(\uparrow)$ reaches the leading edge of the airfoil as shown in the Figure 3.2. This region gives rise to leading edge vortex at $\alpha \approx 14.4^0(\uparrow)$ and it grows in size till $\alpha \approx 16.9^0(\uparrow)$ as shown in the Figure 3.5 and Figure 3.6. The corresponding increase in lift force is observed from Figure 3.14. The main leading vortex grows to critical size sufficient to move at a higher velocity as it detaches from the surface and begins to convect downstream over the suction

surface of the airfoil till it reaches the maximum amplitude of the pitching cycle. The slope of the lift coefficient curve increases visibly from $\alpha \approx 16.9^0(\uparrow)$ and continues to increase as the main leading edge vortex grows in size until it is shed from the suction surface of the airfoil.

The average vortex convective velocity up to this point is approximately $0.28U_\infty$. As the main vortex reaches the trailing edge, the flow from the pressure side of the airfoil at the trailing makes a turn towards the suction side due to the negative pressure of the main vortex forming a counter rotating trailing edge vortex as shown in the Figure 3.7.

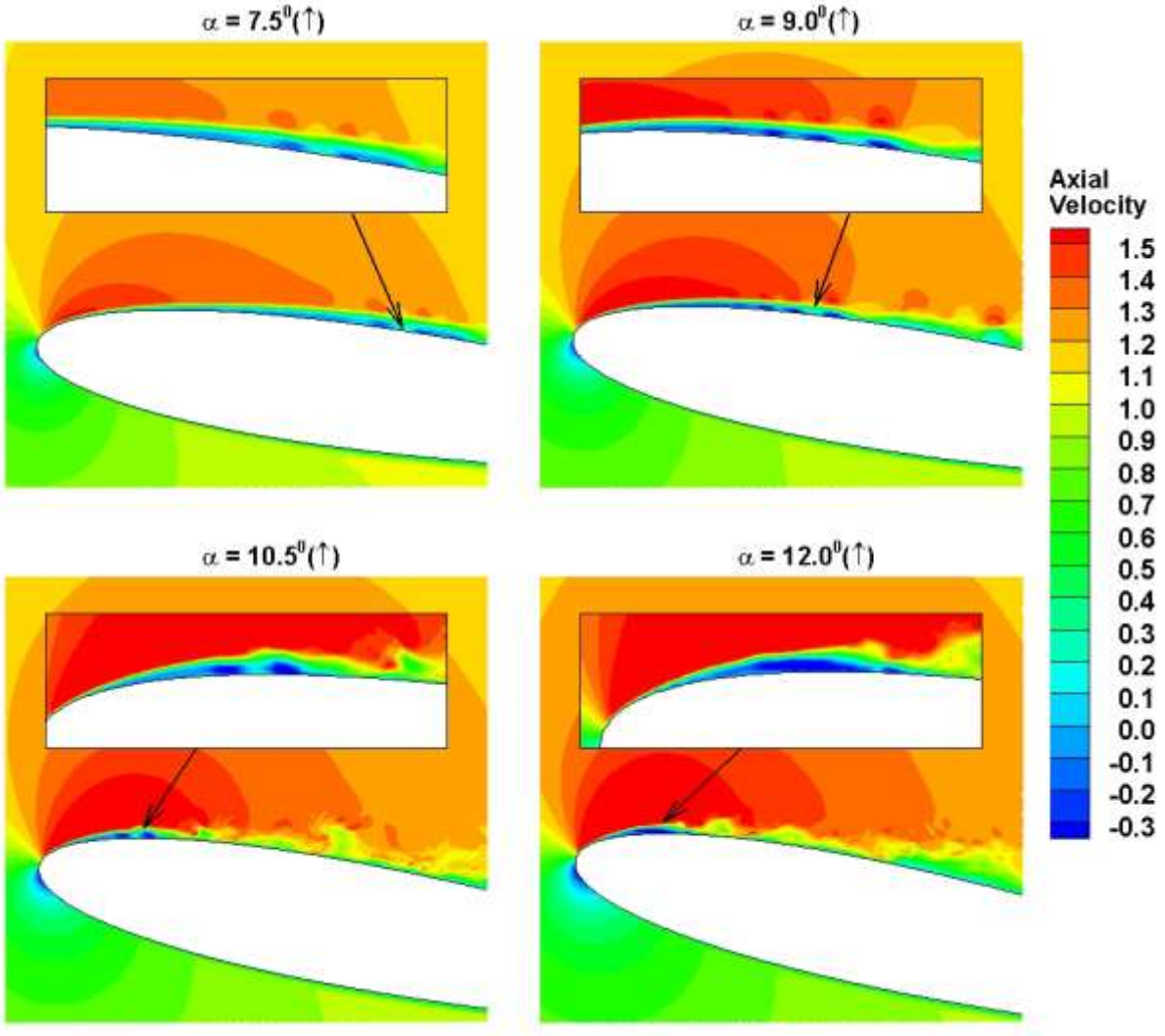

Figure 3.2: Formation of the Main Leading Edge Vortex during Upstroke

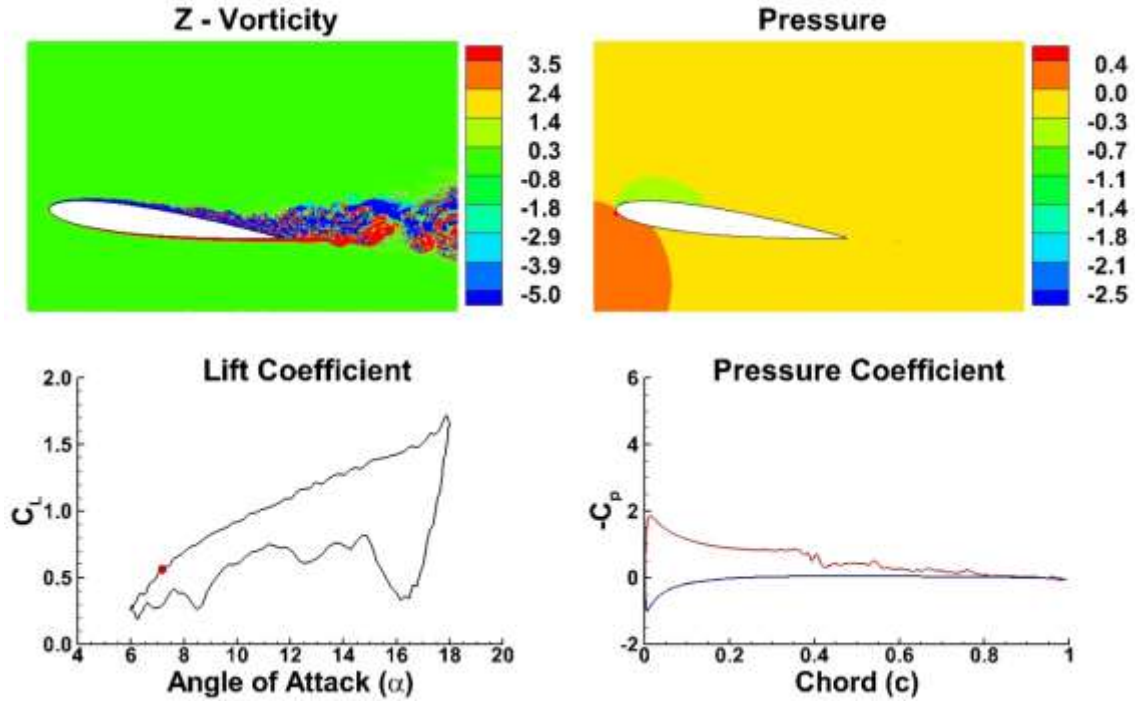

Figure 3.3: Flow Field and Pressure Coefficient Plot at α = 7.2° (↑)

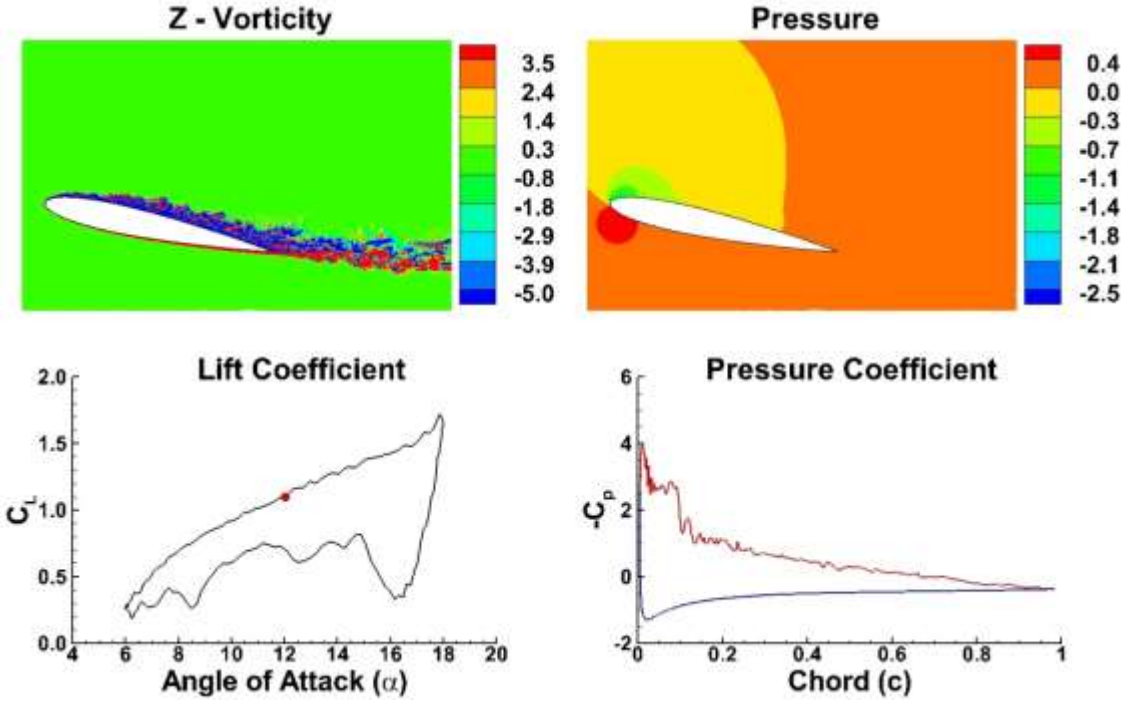

Figure 3.4: Flow Field and Pressure Coefficient Plot at α = 12° (↑)

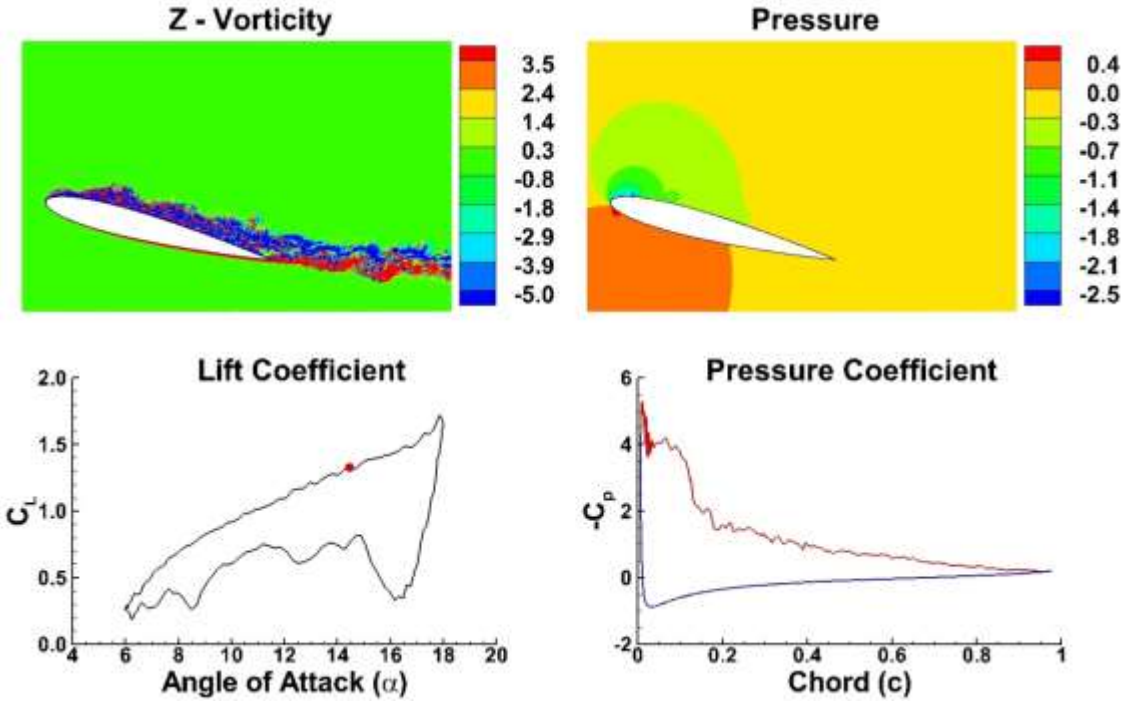

Figure 3.5: Flow Field and Pressure Coefficient Plot at α = 14.4° (↑)

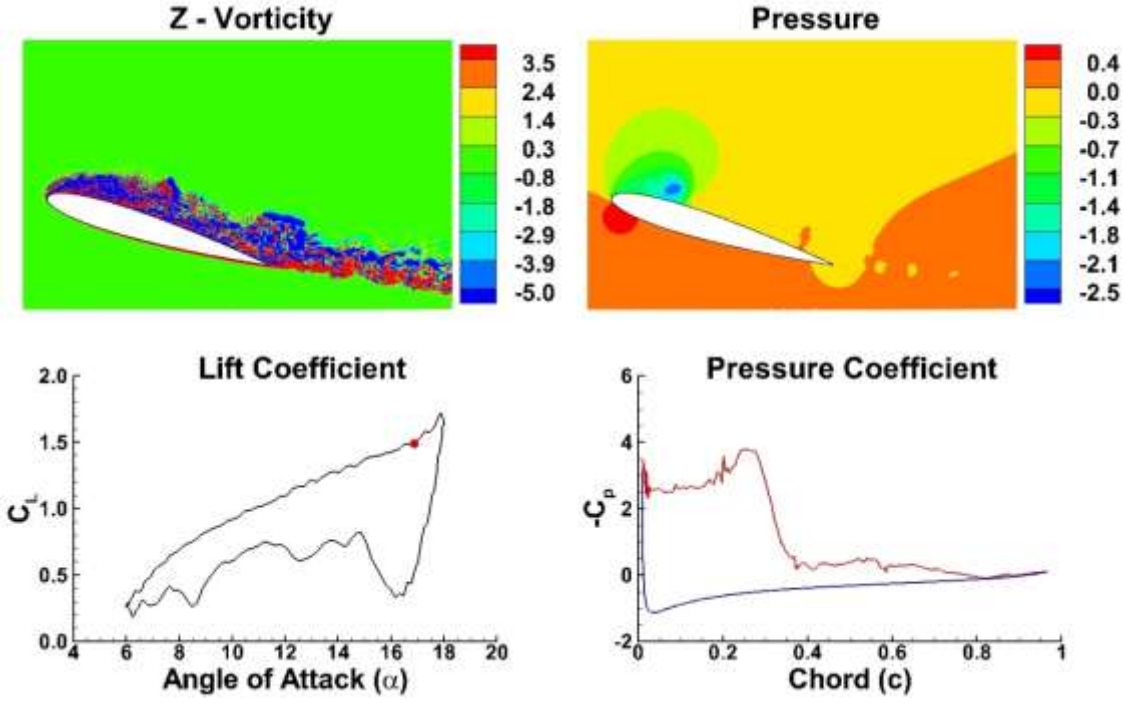

Figure 3.6: Flow Field and Pressure Coefficient Plot at α = 16.9° (↑)

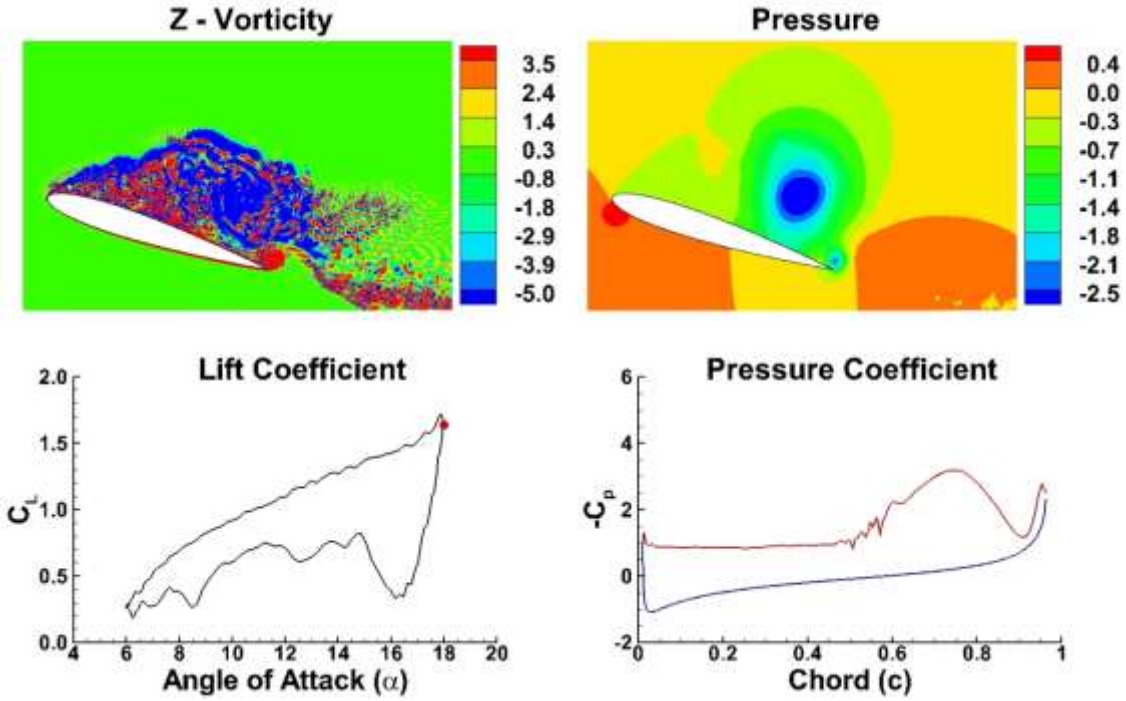

Figure 3.7: Flow Field and Pressure Coefficient Plot at α = 18°

The further movement of the leading edge vortex along the surface of the airfoil is hindered by the formation of the trailing edge vortex and thus it starts to shed from the surface of the airfoil. This incident happens at the maximum amplitude of the pitching cycle ($\alpha = 18^0$). The trailing edge vortex grows in size as the main vortex sheds and travels away from the airfoil surface from $\alpha = 18^0$ to $\alpha \approx 17.2^0$ downstroke (↓) as shown in the Figure 3.8 and the lift coefficient drops to 0.9 due to shedding of the main leading edge vortex. The lift coefficient further drops to 0.332 at $\alpha \approx 16.5^0(\downarrow)$ as the trailing vortex also sheds from the airfoil surface as shown in the Figure 3.9. After the trailing edge vortex sheds from the airfoil surface, several weak vortices of varying intensity are generated at the leading edge from $\alpha \approx 16.5^0(\downarrow)$ to $\alpha \approx 7.6^0(\downarrow)$ and are convected downstream of the airfoil as shown in the Figure 3.10 and Figure 3.11. Flow reattachment process starts at $\alpha \approx 7.2^0(\downarrow)$ and is completed at $\alpha \approx 7.2^0(\uparrow)$. The complete airfoil suction surface remains stalled from $\alpha \approx 18^0$ to $\alpha \approx 7.2^0(\downarrow)$ as shown in Figure 3.12. The summary of the vortex structures development for this particular case (where $Re_c = 10^5$ and $k = 0.188$) is provided in the Figure A. 1.

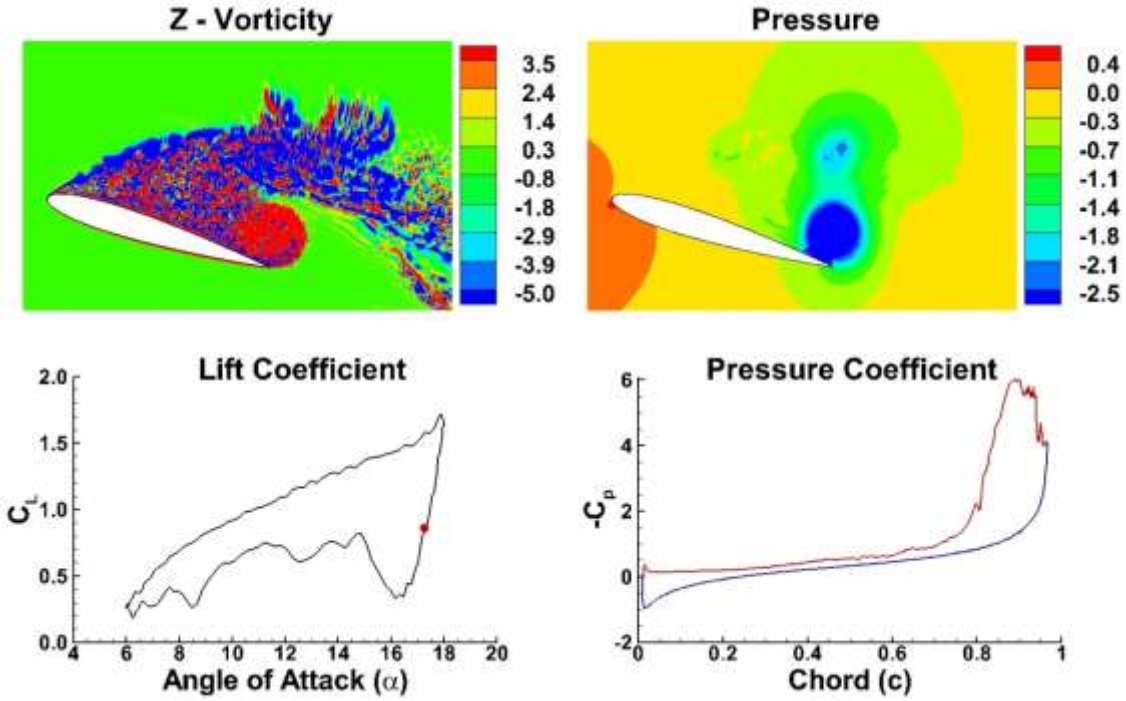

Figure 3.8: Flow Field and Pressure Coefficient Plot at α = 17.2° (↓)

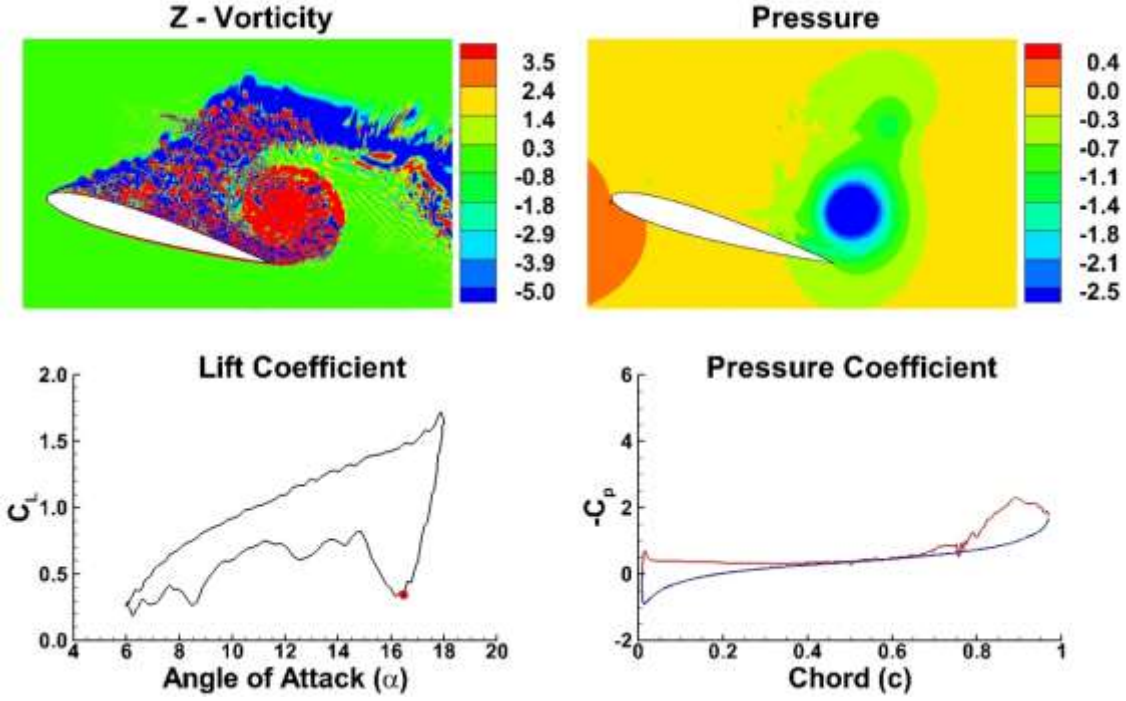

Figure 3.9: Flow Field and Pressure Coefficient Plot at α = 16.5° (↓)

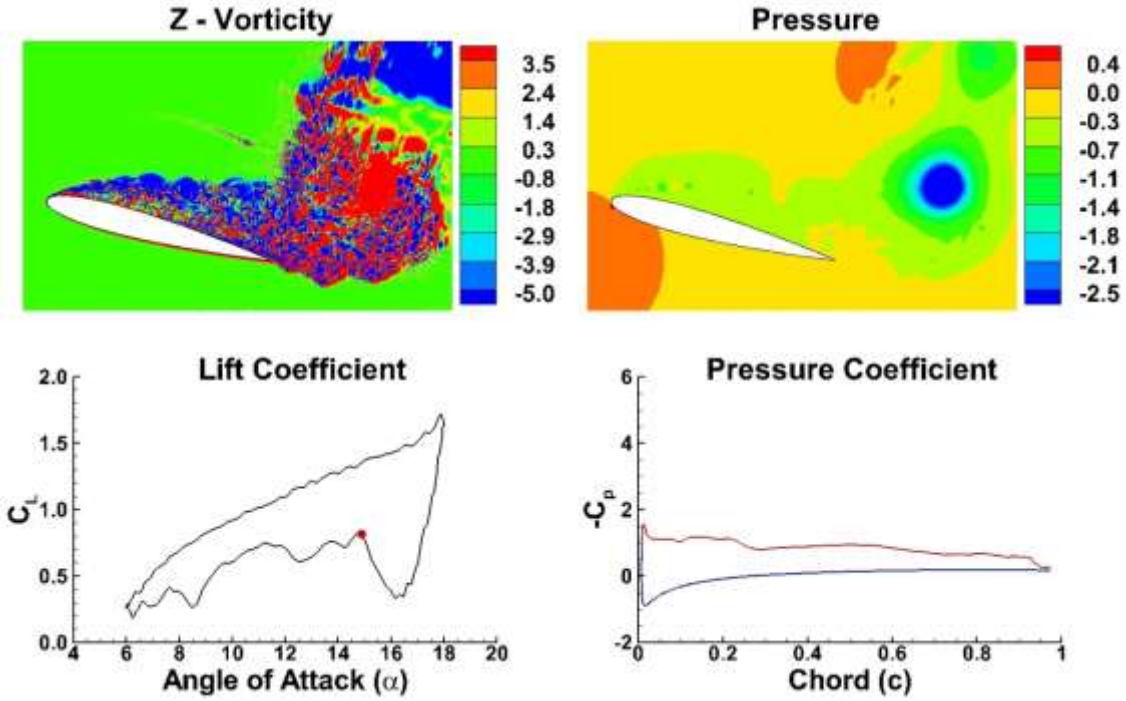

Figure 3.10: Flow Field and Pressure Coefficient Plot at $\alpha = 14.9°$ (↓)

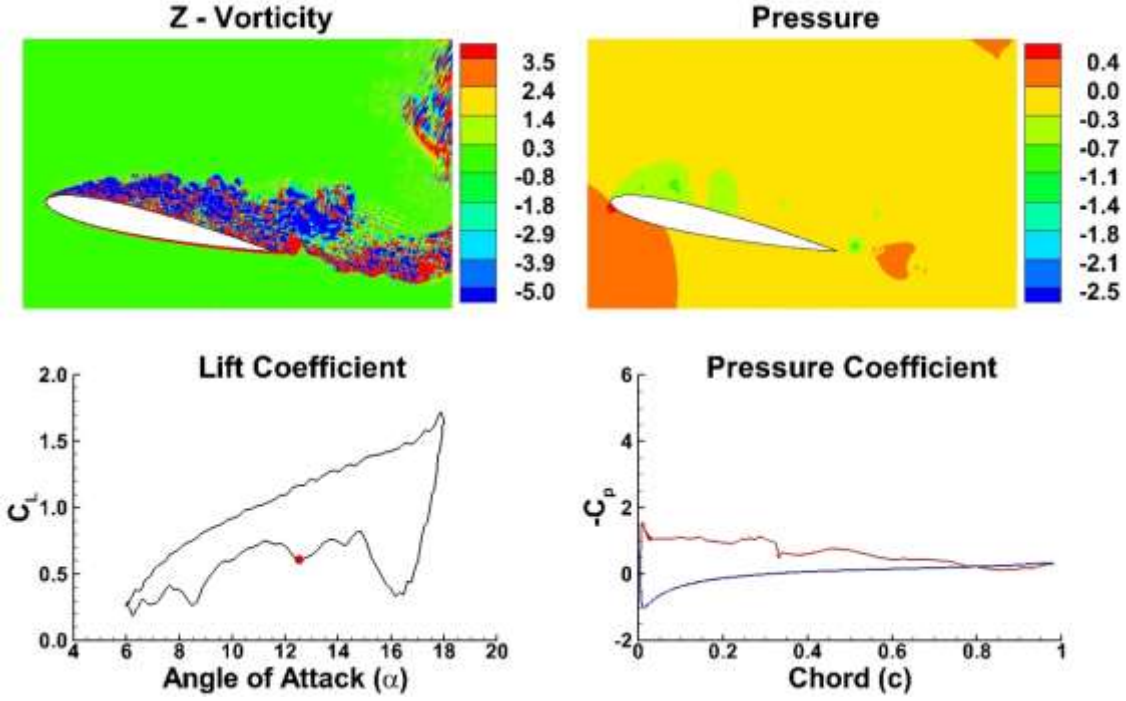

Figure 3.11: Flow Field and Pressure Coefficient Plot at $\alpha = 12.5°$ (↓)

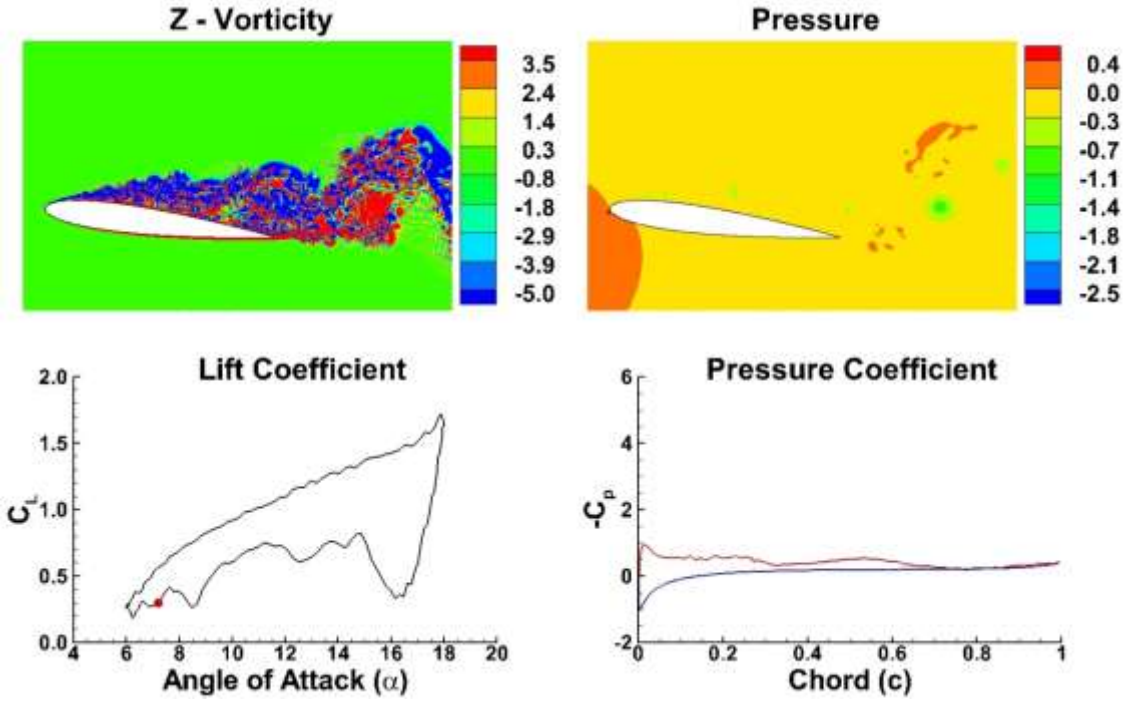

Figure 3.12: Flow Field and Pressure Coefficient Plot at α = 7.2° (↓)

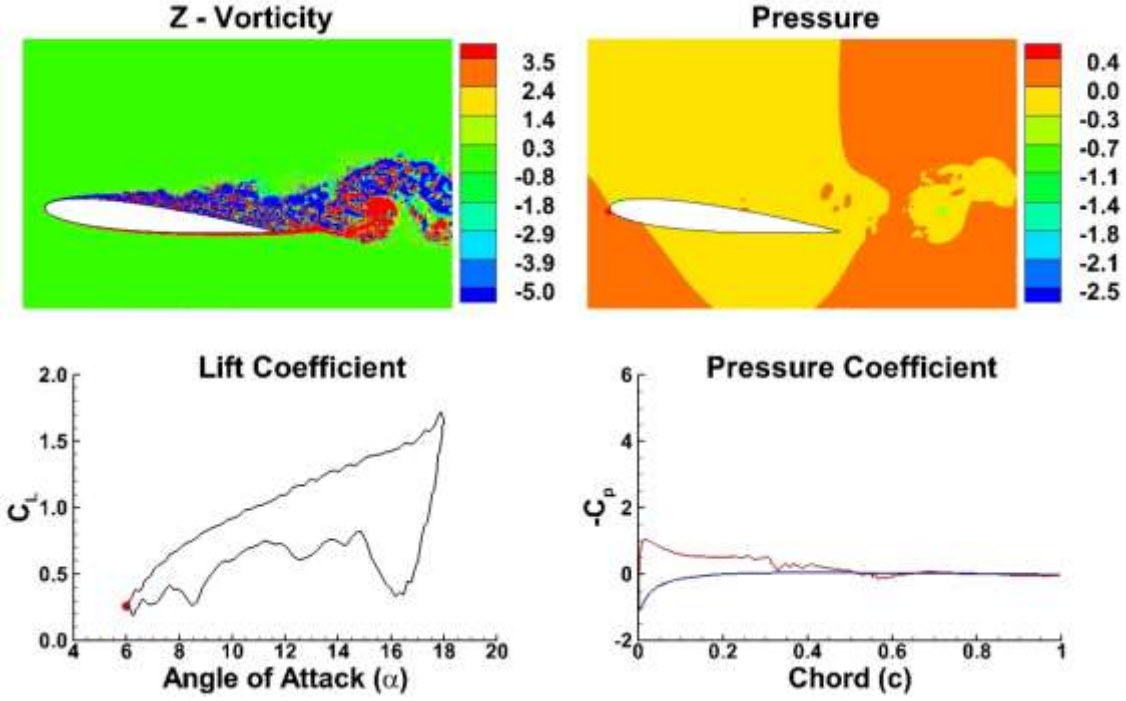

Figure 3.13: Flow Field and Pressure Coefficient Plot at α = 6°

3.4 Comparison with Experiments

The present simulations are compared with the experiments and the lift hysteresis comparison plot is shown in the Figure 3.14. The lift hysteresis plot is generated from the instantaneous data of the second pitching cycle. The phase-averaged lift coefficients are not calculated due to excessive CPU time requirements of the present simulation. The lift coefficient predicted from the present simulation agrees well with the experiments during the upstroke. Simulations under-predict the lift coefficient as compared to the experiments at the start of the downstroke and the additional drop in the lift coefficient can be attributed to the shedding of the trailing edge vortex along with the main leading edge vortex.

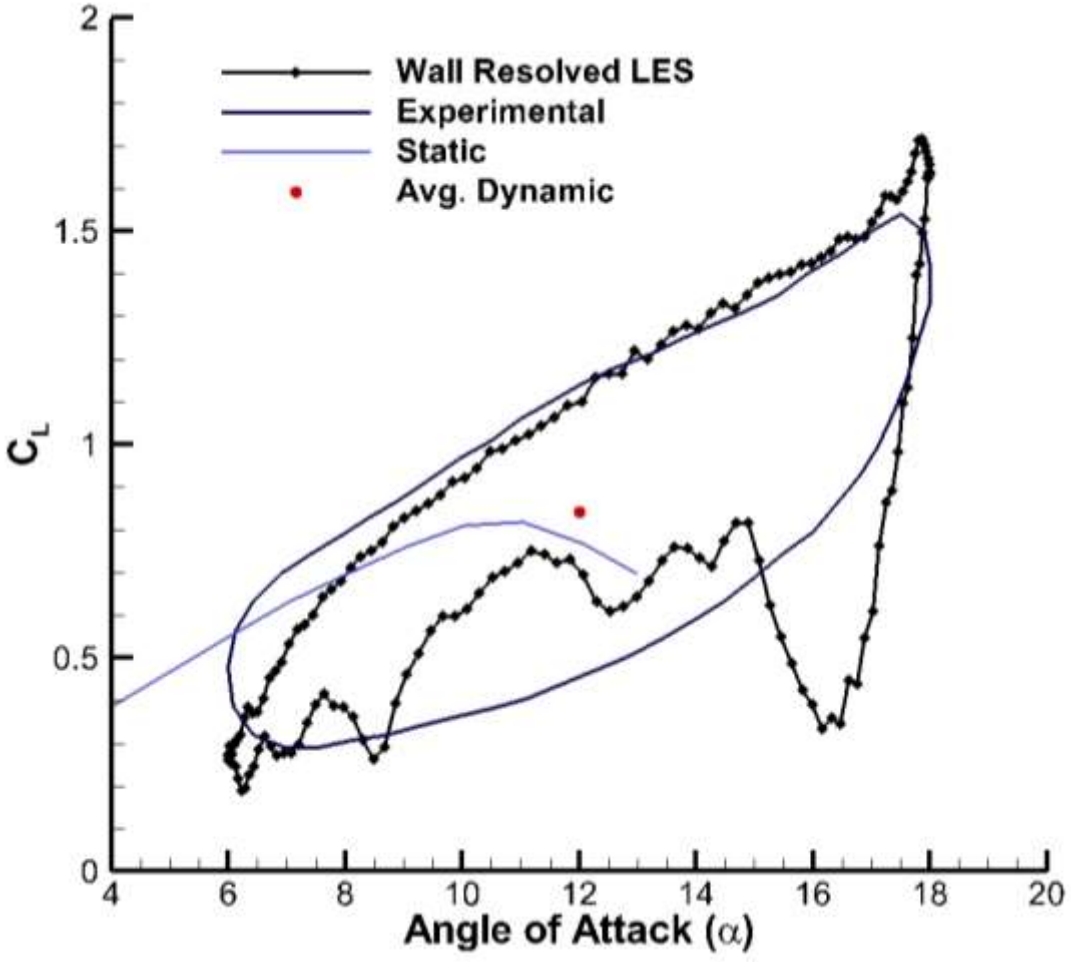

Figure 3.14: Lift Hysteresis Comparison Plot of the Computations with the Experiments at Re = 10^5

The lift coefficient is over estimated for the remaining portion of the downstroke due to the formation of the weak leading edge vortices after the main leading edge vortex and counter rotating trailing edge vortex are shed from the suction surface of the airfoil. The flow remains separated at the trailing edge at the minimum amplitude of the pitching cycle and flow attachment process continues at the start of upstroke till $\alpha \approx 7.2^0$.

The main vortex and trailing edge vortex are shed from the airfoil suction surface at an angle to the free stream direction as shown in the Figure 3.8 through Figure 3.10. As the test section dimensions are smaller in comparison to the airfoil chord length in the experiment (walls of the test section are only approximately 3 chord lengths away from the airfoil trailing edge as compared to the 15 chord lengths in the computational domain) and the flow is subsonic, it could have an impact on the pressure distribution on the suction surface of the airfoil and thus the lift coefficient during the vortex shedding process. The average dynamic stall lift coefficient is shown is shown in the red dot in the Figure 3.14 and is slightly higher than its static counterpart. The average dynamic stall lift coefficient increases with increasing pitching frequency.

3.5 Conclusions

In this study, three dimensional simulations of dynamic stall phenomenon of flow over NACA0012 airfoil at $Re_c = 10^5$ and $k = 0.188$ using wall resolved large eddy simulations are performed. Detailed development of events leading to dynamic stall and the lift hysteresis comparison plot are presented. The possible reasons for the difference in the lift coefficient result between simulation and experiment are provided. There is a fairly good match between the predicted and experimentally measured lift coefficient during the upstroke. Although the net lift coefficient during downstroke matches with the experimental data, the present study under-predicts the lift coefficient as compared to the experimental values at the start of downstroke and over-estimates for the remaining part of the downstroke. The differences between the simulation results and the experimental data during the downstroke of the pitching cycle can possibly be attributed to the domain dependency of the results in the experiments. The simulations also show that

the reattachment process of the stalled airfoil extends into the start of the upstroke in the subsequent cycle due to low reduced frequency of the pitching cycle.

4. Dynamic Stall Simulation of Re = 10^6 case

This chapter discusses in detail about the dynamic stall simulation of flow over NACA0012 airfoil at 10^6 Reynolds number and at reduced frequency of $k = 0.25$. The first section of this chapter provides the details of the experimental setup from which the data is compared with the present simulation results. The next section provides the simulation details and subsequently the simulation results are discussed. The last two sections provide the comparison of the simulation results with the experimental data and conclusions from the present study.

4.1 Experimental Setup

The flow over a pitching NACA0012 airfoil was experimentally investigated at 10^6 Reynolds number based on the chord length over a range of reduced frequencies.[4] Hot wire probes and surface pressure transducers were used to identify the influence of laminar separation bubble in the growth and shedding of the main stall vortex and to measure the resultant aerodynamic loads.

The experiment was conducted in the AMRDL-Ames 7×10 ft. subsonic wind tunnel to obtain detailed information about the NACA0012 airfoil operating conditions that produce dynamic stall. The reduced frequency (k) was varied from 0.05 to 0.25. The airfoil was arranged such that the pitching sinusoidal motions could be about the axis that is at the quarter chord from the leading edge. Most of the data recorded was for the $15^0 \pm 10^0$ airfoil mean angle of attack and amplitude combination. The emphasis of measurements were two fold – hot wire anemometer and pressure transducer measurements near the leading edge region to better understand the role of laminar separation bubble in the overall dynamic stall phenomenon, and to obtain pressure measurements over the surface of the airfoil to quantify the aerodynamic coefficients.

The airfoil dimensions were 1.22 m. × 1.98 m. in the chord-wise and span-wise directions respectively. The airfoil was mounted vertically between the end plates spanning the test section. The model was fabricated around a tubular spar which was supported below the ground plane by a pivot

bearing and above the ceiling by a sleeve bearing. Two identical pitot-static probes were located upstream of the model to provide an instantaneous measure of the dynamic pressure in the test section and to serve as the source of total pressure to be used as a reference for all differential pressure transducers. The static pressure measurements were performed at 10 locations (with 7 of those in the 10% chord from the leading edge) on both the upper and lower side of the airfoil along the chord-wise stations. Both the steady and unsteady pressure distributions had been measured on each side of the wing surface at the mid-span location. The normal force and pitching moment coefficients are calculated by ensemble-averaging for 100 cycles and then integrating these pressures over the airfoil.

4.2 Simulation Details

The equations are solved in a finite volume framework on a block structured, boundary fitted and non-staggered grid using a fractional step algorithm for time advancement. Second order central difference with upwind limiter is used for spatial discretization of convective terms and second order central differencing is used for the discretization of the viscous terms and implicit Crank-Nicolson scheme is used for advancement in time.

The forced unsteadiness is generated on the airfoil by means of pitching motion around the quarter chord axis and is defined by the time-dependent angle of attack (α), as shown in the is given as:

$$\alpha = \alpha_{\min} + \frac{1}{2}(\alpha_{\max} - \alpha_{\min})(1 - \cos 2kt) \quad \textbf{(4.1)}$$

For this simulation, the angle at the minimum amplitude is $\alpha_{\min} = 5^0$ and the angle at the maximum amplitude is $\alpha_{\max} = 25^0$ oscillating about the mean angle of attack $\alpha_m = 15^0$ $(i.e.\ 15^0 \pm 10^0)$. The reduced frequency of the pitching motion (k) is taken as 0.25.

The initial transient field is generated at the minimum angle of attack $(i.e.\ \alpha_{min} = 5^0)$ by simulating the flow over static airfoil at α_{min} for 8 flow through time units over the length of the airfoil. The oscillatory motion is then introduced and the unsteady flow field is computed by marching in time. The

dynamic stall results are reported after simulating for more than two pitching cycles and repeatability in results are observed.

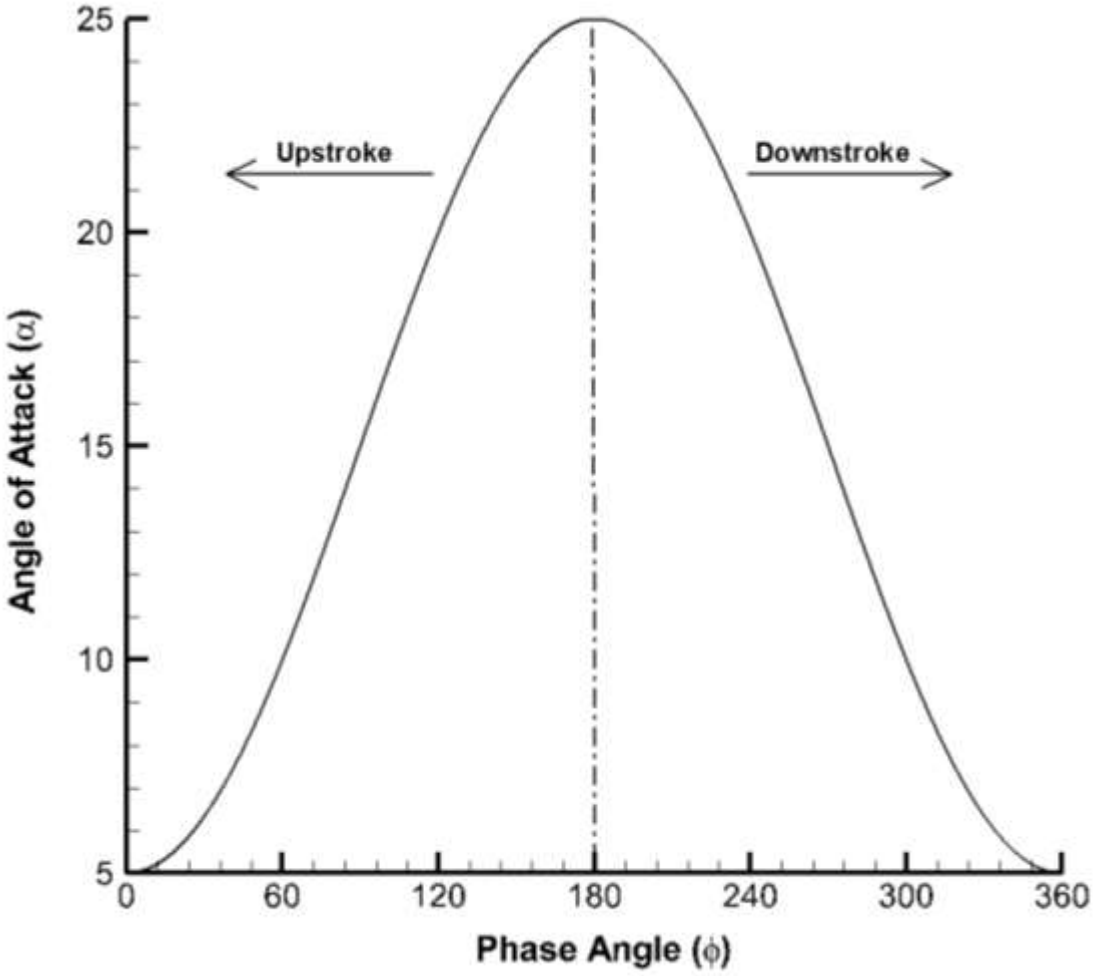

Figure 4.1: Input Angle of Attack Wave Form with Phase Angle for Re = 10^6 case

4.3 Results

The development of the unsteady flow field is shown in the Figure 4.2 through Figure 4.16. In the initial part of the upstroke, the flow is fully attached to the suction surface of the airfoil from $\alpha = 5^0$ to $\alpha \approx 19.2^0$ as shown in the Figure 4.2 through Figure 4.4.

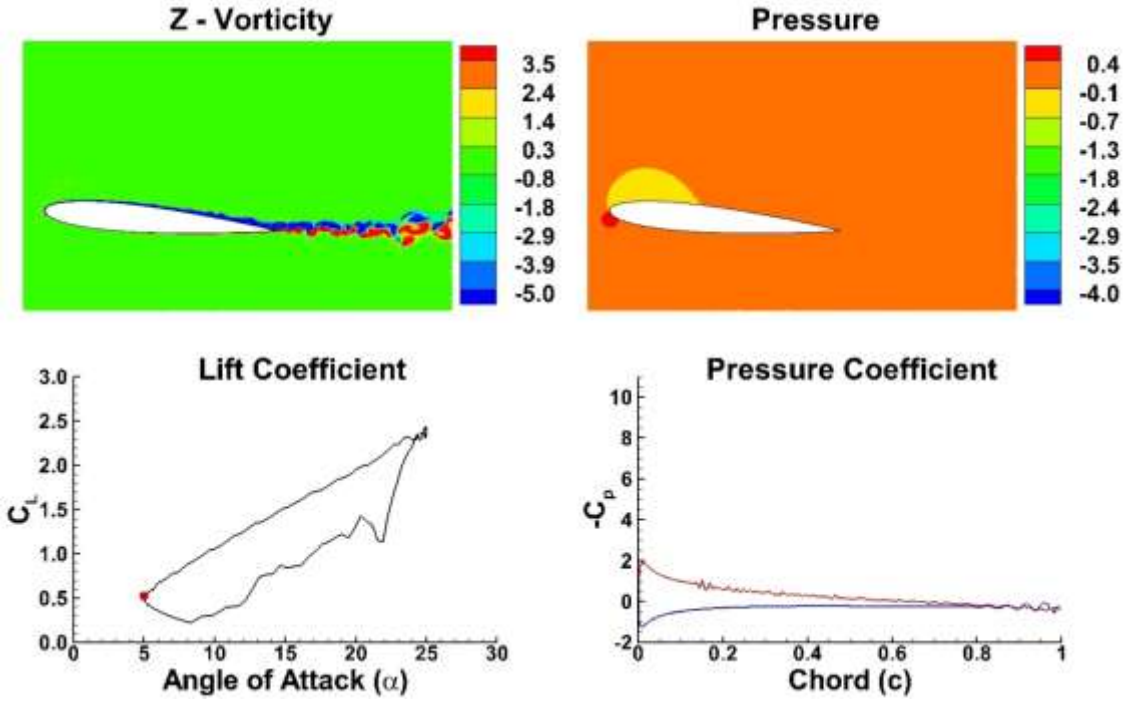

Figure 4.2: Flow Field and Pressure Coefficient Plot at α = 5°

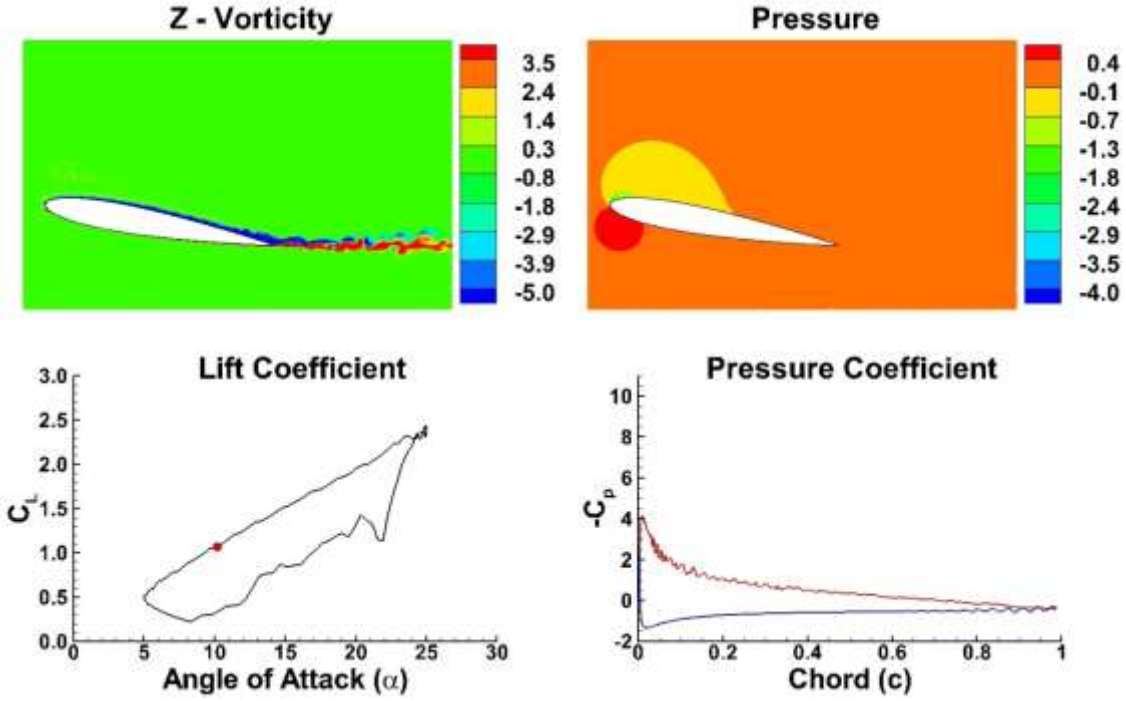

Figure 4.3: Flow Field and Pressure Coefficient Plot at α = 10.2° (↑)

Therefore the airfoil is in the linear lift regime during the upstroke from $\alpha = 5^0(\uparrow)$ to $\alpha \approx 20^0(\uparrow)$ (See Figure 4.17). Unlike the case in the previous chapter ($i.e. Re_c = 10^5$), a shallow separation bubble is observed at the leading edge itself at $\alpha \approx 19.2^0(\uparrow)$ as shown in the Figure 4.5 and the vortex becomes visibly apparent at $\alpha \approx 20.9^0(\uparrow)$ near 10% of the chord as shown in the Figure 4.6. Thus the slope of the lift coefficient curve increases as a result of the negative pressure due to the vortex formation on the airfoil suction surface. The main leading edge vortex moves to 20% of the chord at $\alpha \approx 23^0(\uparrow)$ and grows to a critical size sufficient for advection along the airfoil suction surface as shown in the Figure 4.7. Because of the increased vortex strength, at $\alpha \approx 23^0(\uparrow)$ there is again a noticeable increase in the slope of the lift curve.

Although the main leading edge vortex moves downstream and gains strength, its effect on the suction surface of the airfoil is less as compared to the previous case because the vortex core moves away from the suction surface of the airfoil as the major portion of the vortex movement on the airfoil surface happens during the downstroke and this phenomenon can be observed from Figure 4.8 to Figure 4.10.

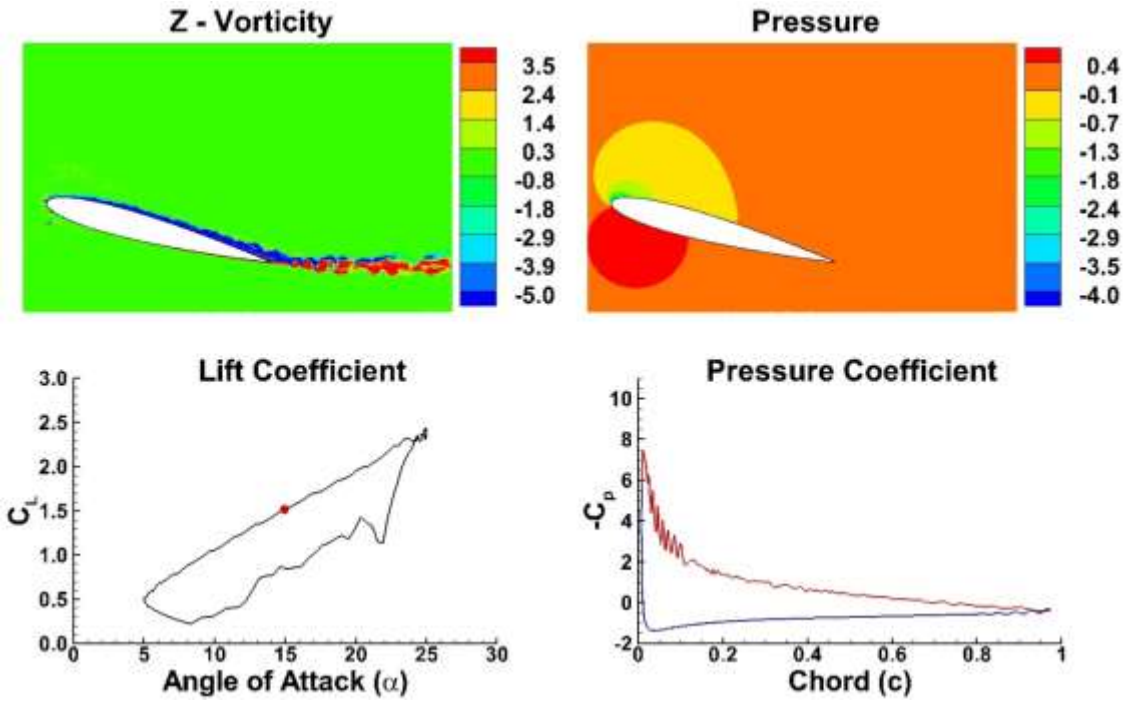

Figure 4.4: Flow Field and Pressure Coefficient Plot at α = 15° (↑)

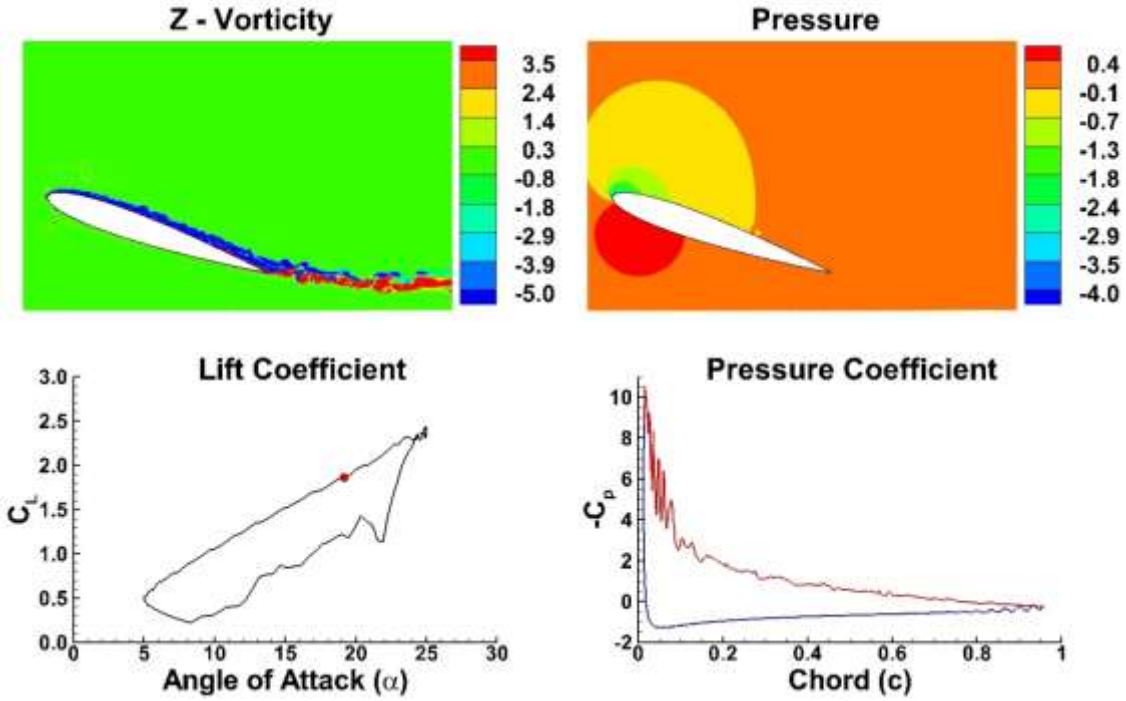

Figure 4.5: Flow Field and Pressure Coefficient Plot at α = 19.2° (↑)

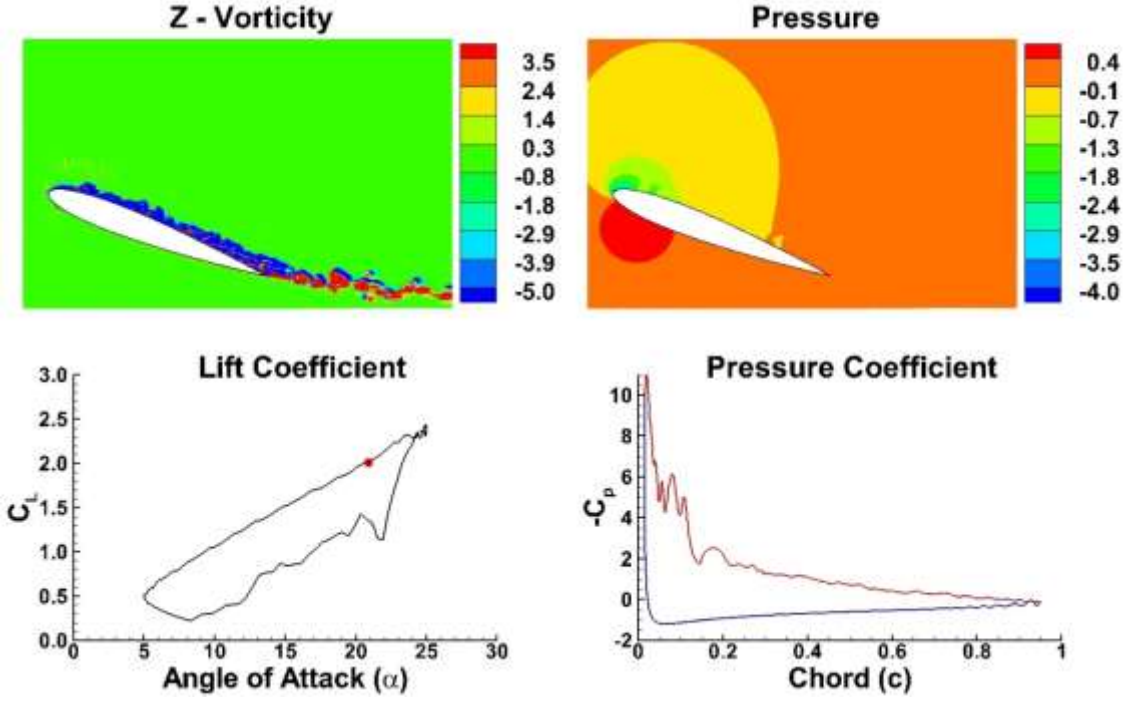

Figure 4.6: Flow Field and Pressure Coefficient Plot at α = 20.9° (↑)

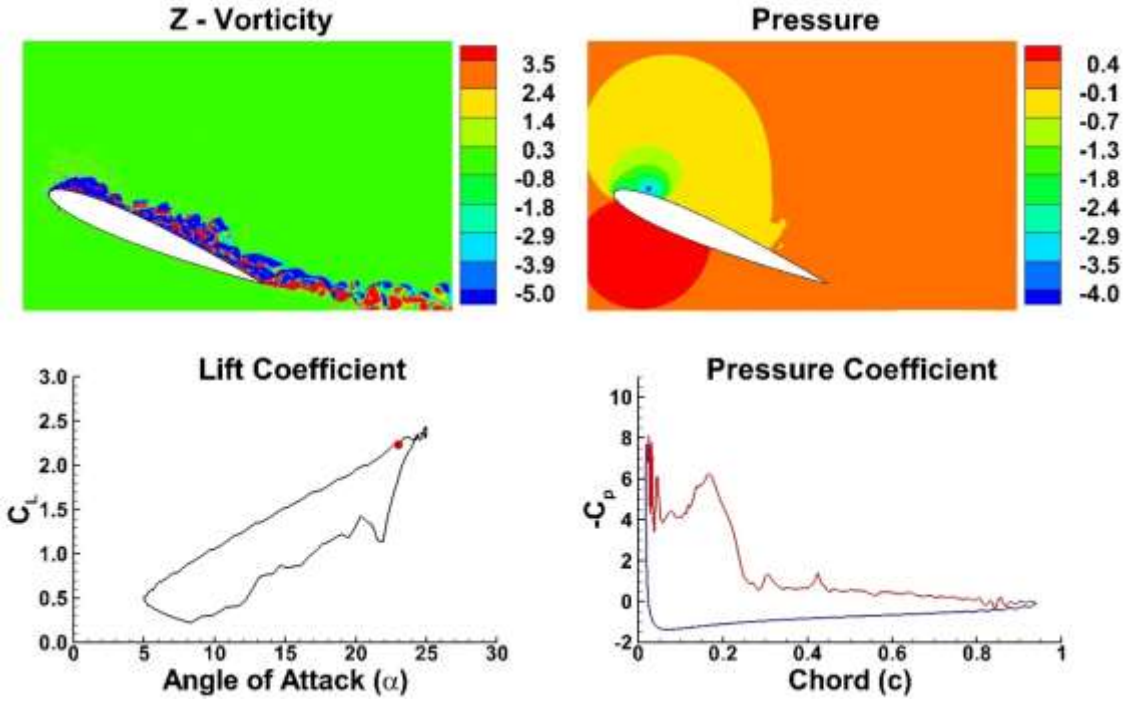

Figure 4.7: Flow Field and Pressure Coefficient Plot at α = 23° (↑)

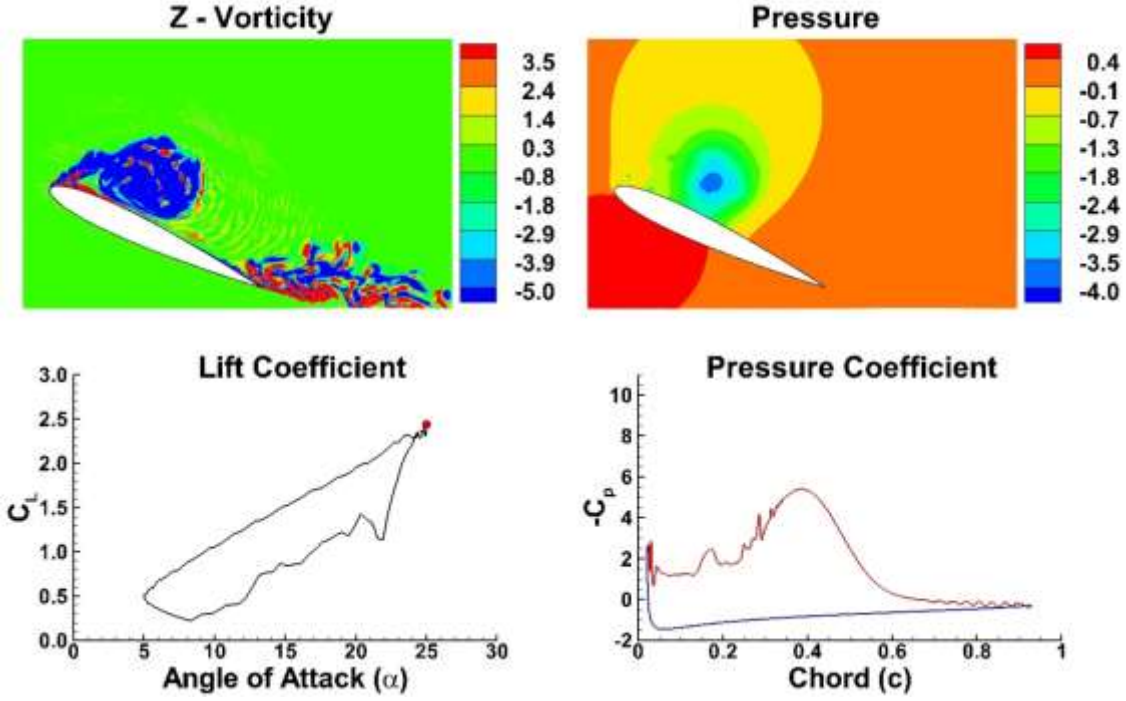

Figure 4.8: Flow Field and Pressure Coefficient Plot at α = 25°

The vortex convects downstream to 40% of the chord at the maximum amplitude of the pitching cycle. Although the extent of the spread of negative pressure due to the size of the main leading edge vortex increases from $\alpha \approx 23^0(\uparrow)$ to $\alpha = 25^0$, the maximum vortex suction peak on the upper airfoil surface remains almost constant. As a result, the lift coefficient remains almost constant from $\alpha \approx 23^0(\uparrow)$ to $\alpha = 24^0(\downarrow)$.

As the main leading edge vortex starts to shed from the airfoil surface at $\alpha = 24^0(\downarrow)$ as shown below in the Figure 4.9, the lift coefficient starts to drop as is also evidenced from the lift hysteresis plot (See Figure 4.17). As the main leading edge vortex sheds away from the airfoil suction surface and convects downstream, the lift coefficient continues to drop till $\alpha \approx 21.9^0(\downarrow)$ when the effect of vortex core reaches the suction surface of the airfoil near the trailing edge. The average vortex convective velocity up to this point is approximately $0.3U_\infty$.

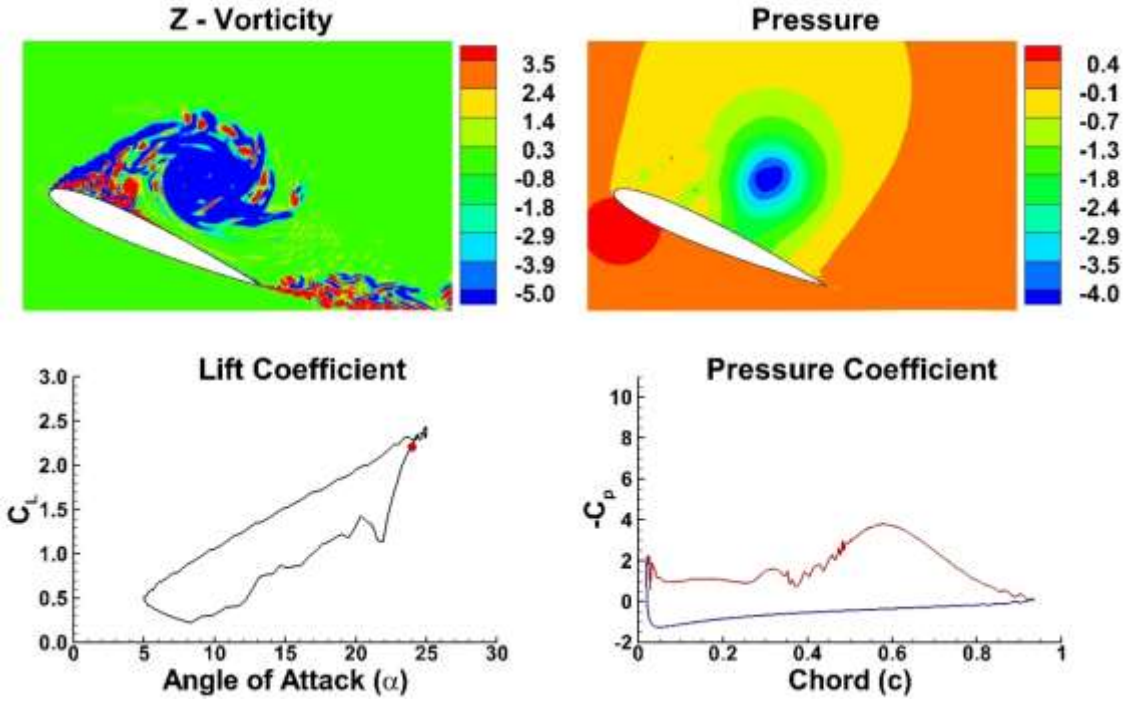

Figure 4.9: Flow Field and Pressure Coefficient Plot at α = 24° (↓)

As the negative pressure because of main vortex movement reaches near the airfoil trailing edge surface, the flow from the pressure side of the airfoil at the trailing makes a turn towards the suction side due to the negative pressure of the main vortex forming a counter rotating trailing edge vortex as shown in the Figure 4.10. The intensity of the counter rotating trailing edge vortex is lesser in this case as compared to the case in previous chapter because of the location of the main leading edge vortex. In this case the core of the main leading edge vortex is farther from the airfoil suction surface and one should note that closer the main vortex location is, stronger is the pull of the fluid from the pressure surface of the airfoil.

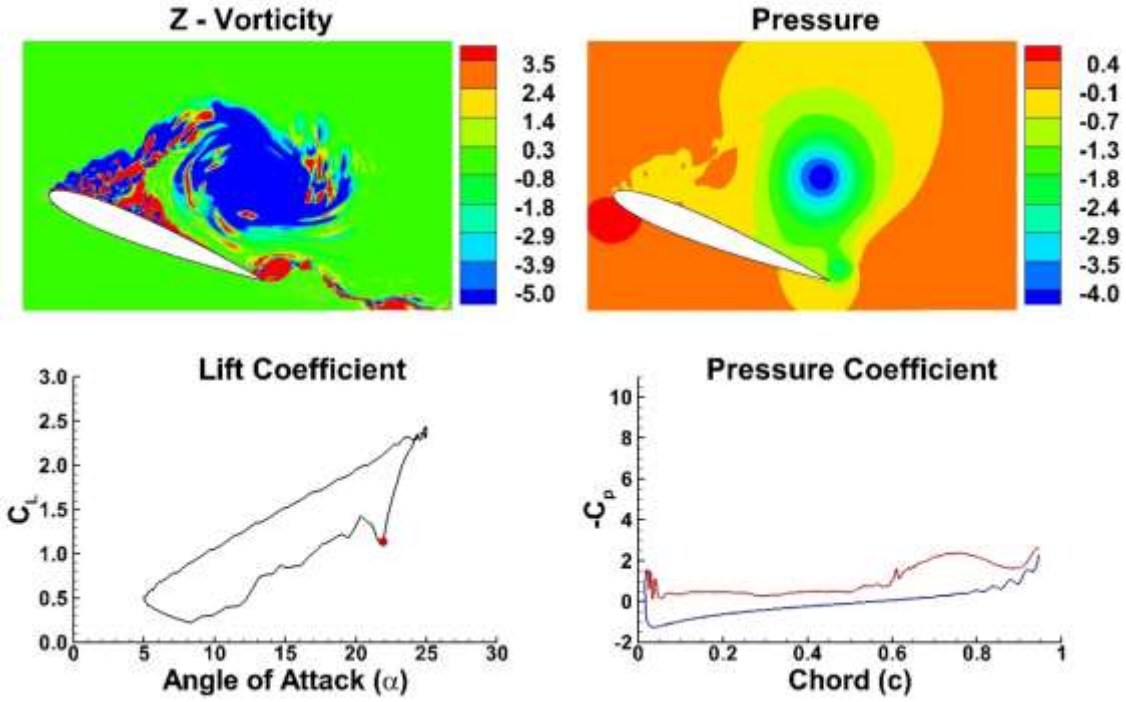

Figure 4.10: Flow Field and Pressure Coefficient Plot at α = 21.9° (↓)

As the main vortex sheds away from the surface, it pulls the counter rotating trailing edge vortex along with it, essentially increasing its size and intensity. The trailing edge vortex moves towards the airfoil trailing edge reverse to the free-stream flow direction and grows in strength as shown in the Figure 4.11.

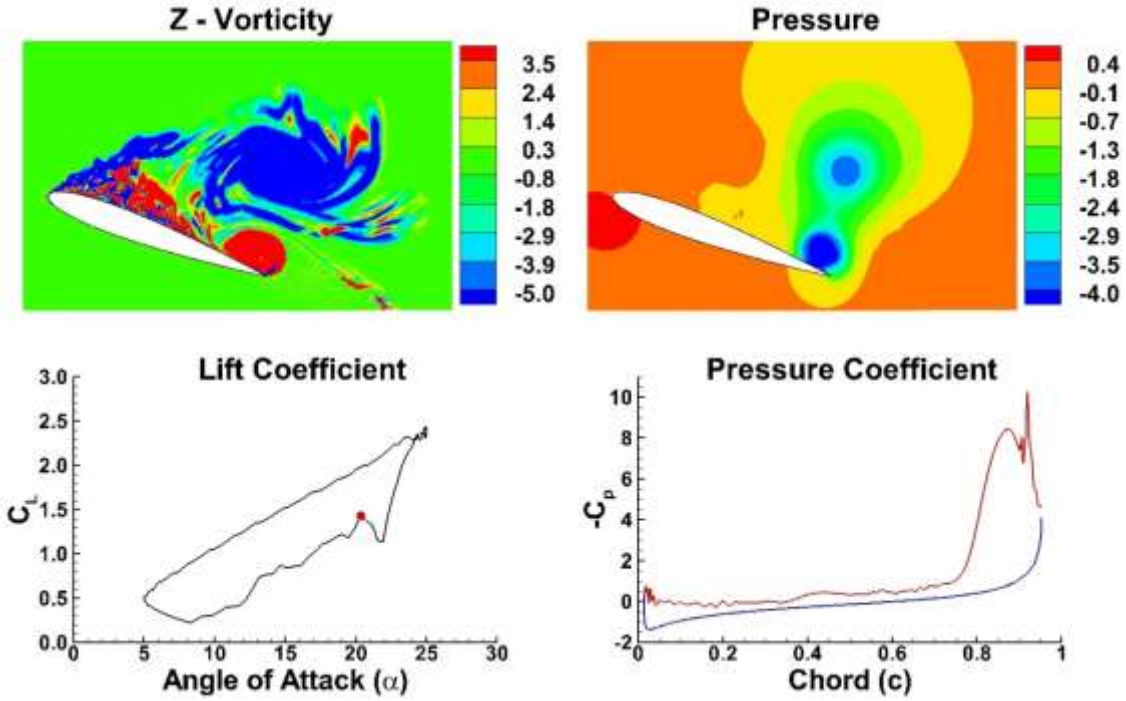

Figure 4.11: Flow Field and Pressure Coefficient Plot at α = 20.3° (↓)

A spike in the negative pressure can be observed on the suction surface near the trailing edge of the airfoil in the pressure coefficient plot in Figure 4.11. Unlike in the previous chapter case where the trailing edge vortex is formed before the main vortex is shed from the airfoil surface, in this case there is no hindrance to the movement of the main leading edge vortex because of the formation of counter rotating trailing edge vortex. Thus the above description explains the difference in trailing edge vortex strengths in both the cases.

The residence time of the trailing edge vortex on the airfoil suction surface near the trailing edge is very small and it sheds immediately following the core of the main vortex. The movement of the trailing edge vortex is always coupled to the movement of the main vortex and this phenomenon can be clearly observed in the Figure 4.12 through Figure 4.14. The formation of the counter-rotating trailing edge vortex for a short time period in the pitching cycle increases the lift coefficient from $\alpha \approx 21.9^0(\downarrow)$ to $\alpha \approx 20.3^0(\downarrow)$.

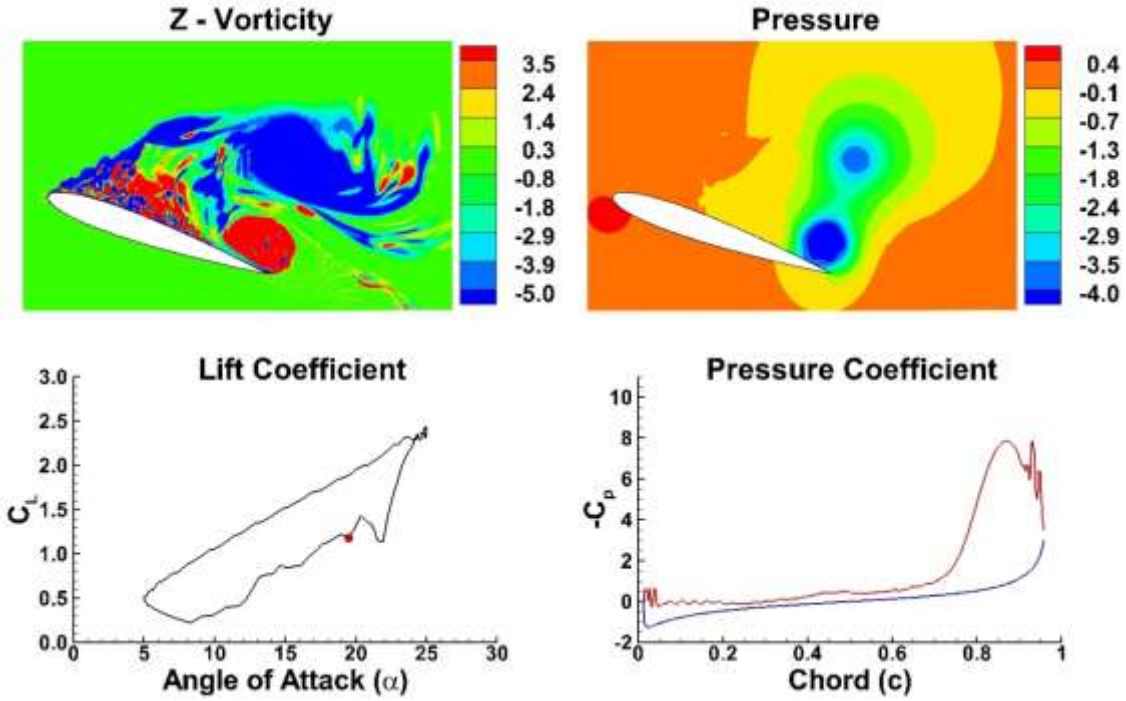

Figure 4.12: Flow Field and Pressure Coefficient Plot at $\alpha = 19.5°$ (↓)

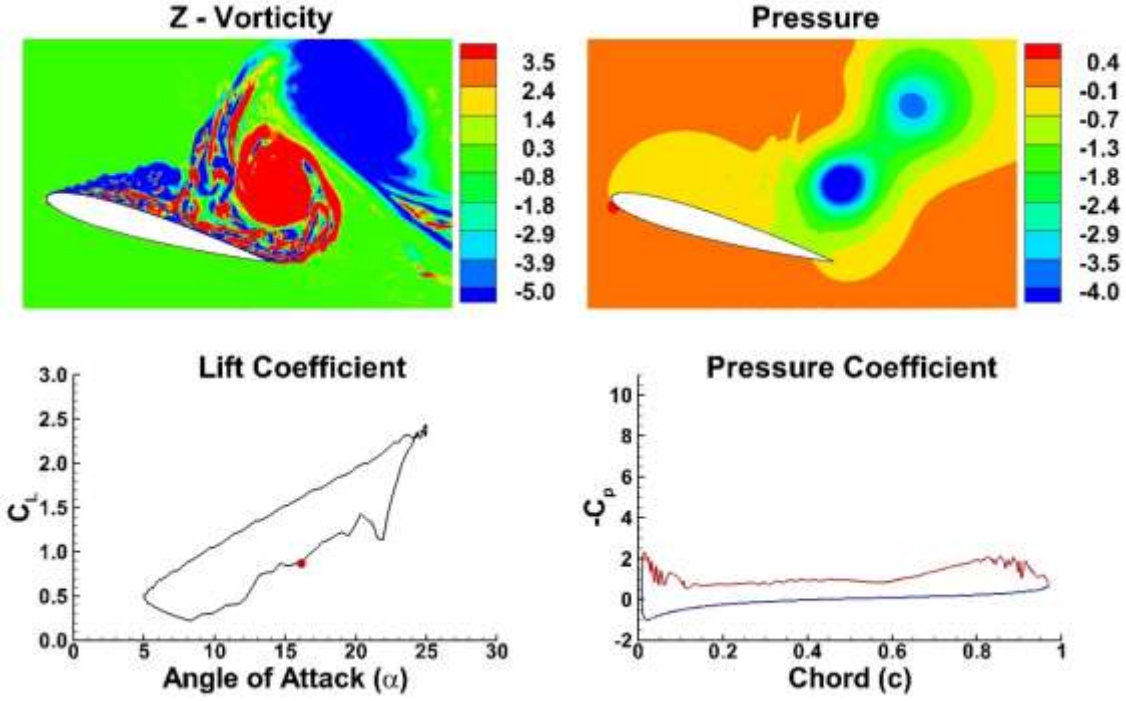

Figure 4.13: Flow Field and Pressure Coefficient Plot at $\alpha = 16.1°$ (↓)

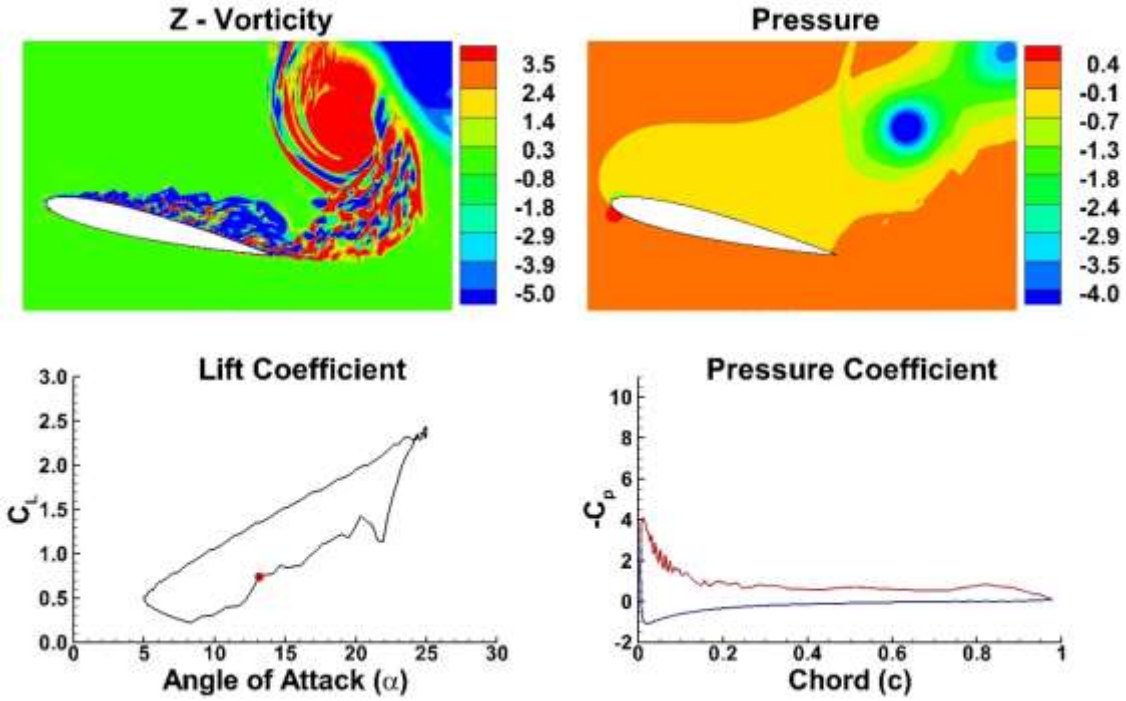

Figure 4.14: Flow Field and Pressure Coefficient Plot at α = 13.1° (↓)

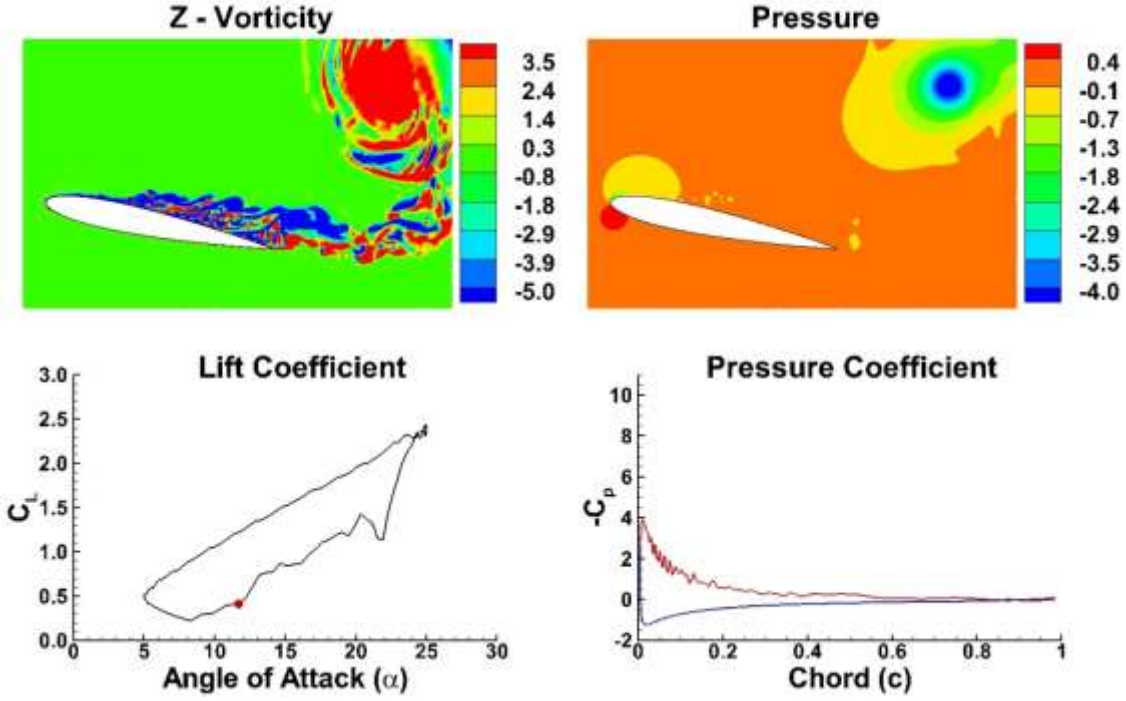

Figure 4.15: Flow Field and Pressure Coefficient Plot at α = 11.7° (↓)

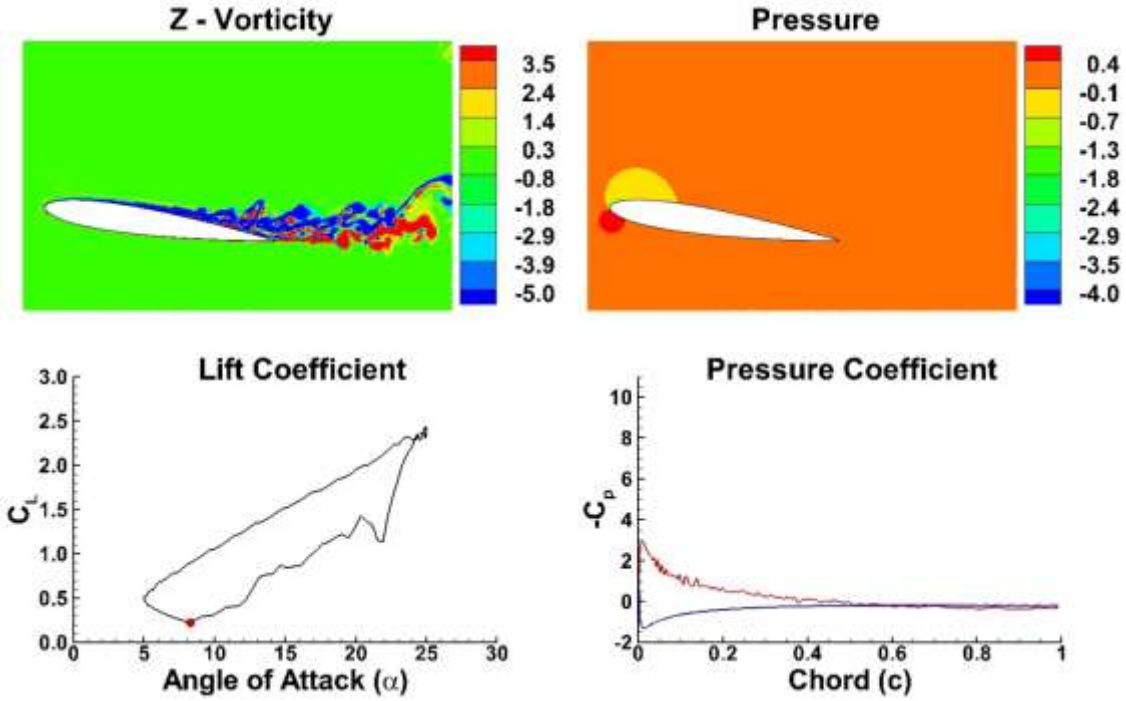

Figure 4.16: Flow Field and Pressure Coefficient Plot at α = 8.3° (↓)

Figure 4.12 to Figure 4.16 show a gradual drop in lift coefficient as the main vortex and the trailing edge vortices convect downstream and away from the airfoil surface. The airfoil remains fully stalled till $\alpha \approx 13^0$ and thereafter the flow starts to reattach from the leading edge. However the aft side of the airfoil remains stalled till $\alpha \approx 8.3^0$ and airfoil becomes fully attached as it reaches the minimum amplitude of the pitching cycle. The summary of the vortex structures development for this particular case (where $Re_c = 10^6$ and $k = 0.25$) is provided in the Figure A. 2.

4.4 Comparison with Experiments

The present simulations are compared with the experiments and the lift hysteresis comparison plot is shown in the Figure 4.17. The lift hysteresis plot is generated from the instantaneous data of the second pitching cycle. The phase-averaged lift coefficients are not calculated due to excessive CPU time requirements of the present simulation. The lift coefficient values fairly match with the experimental data during the upstroke. Simulations under-predict the lift coefficient as compared to the experiments at the

start of the downstroke and the drop in the lift coefficient can be attributed to the shedding of the main leading edge vortex.

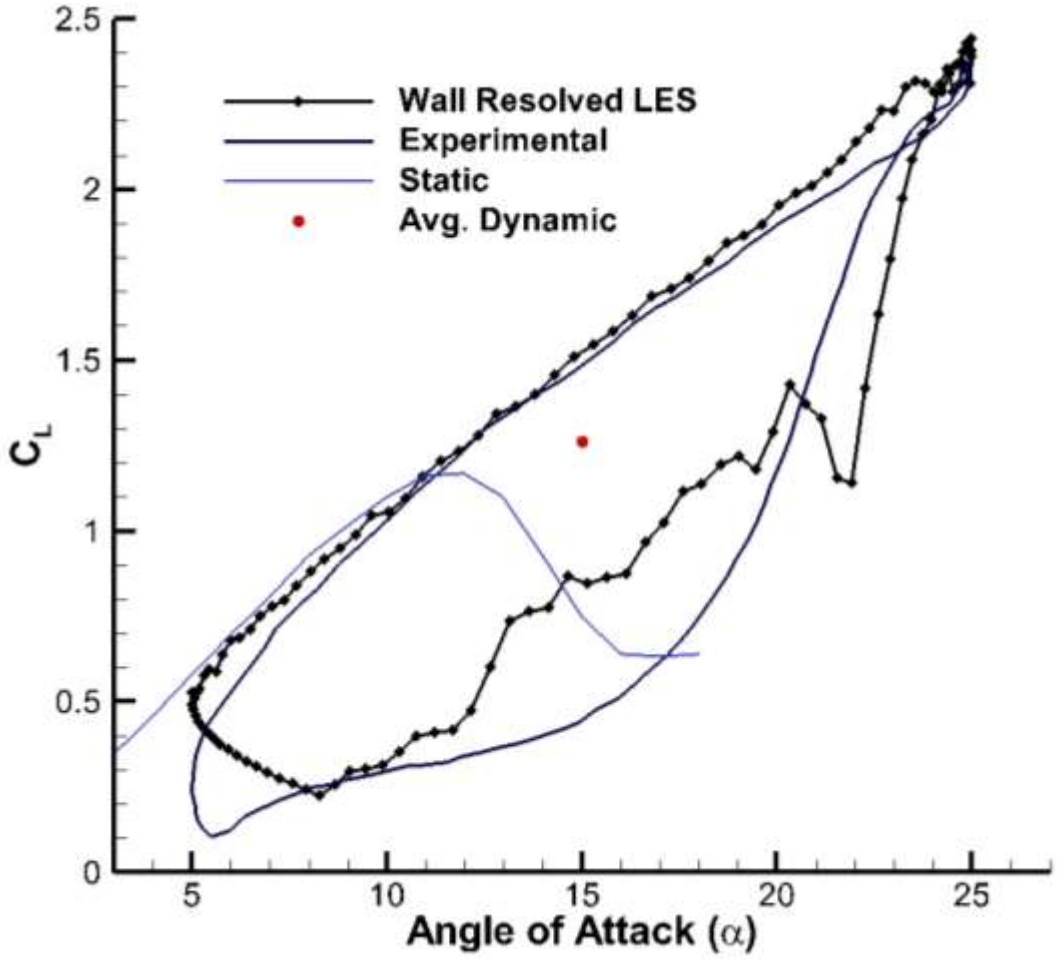

Figure 4.17: Lift Hysteresis Comparison Plot of the Computations with the Experiments at Re = 10^6

The lift coefficient is over estimated for the remaining portion of the downstroke due to the predicted formation of the counter-rotating trailing edge vortex after the main leading edge vortex is shed from the suction surface of the airfoil. Due to convergence problems, a hybrid method of second-order central with first-order upwind limiter is used for the discretization of the convection terms in the Navier-Stokes equations. This over-prediction of the lift coefficient is probably due to the excessive dissipative character of the first-order upwind scheme along with the lower order of accuracy of the discretization scheme that causes the under-estimation of the adverse pressure gradient at high angles of attack leading to the delay

in the prediction of dynamic stall. The average dynamic stall lift coefficient is shown is shown in the red dot in the Figure 4.17 and is significantly higher than its static counterpart. The average dynamic stall lift coefficient increases with increasing pitching frequency.

4.5 Conclusions

In this study, three dimensional simulations of dynamic stall phenomenon of flow over NACA0012 airfoil at $Re_c = 10^6$ and $k = 0.25$ using wall resolved large eddy simulations are performed. Detailed development of events leading to dynamic stall and the lift hysteresis comparison plot are presented. The possible reasons for the difference in the lift coefficient result between simulation and experiment are provided. There is a fairly good match between the predicted and experimentally measured lift coefficient during the upstroke. Although the net lift coefficient during downstroke matches during the downstroke, the present study under-predicts the lift coefficient as compared to the experimental values at the start of downstroke and is over-estimated for the remaining part of the downstroke. It is also observed that as the reduced frequency increases, the flow separation originates at a smaller angle of attack. The simulations also show that the reattachment process of the stalled airfoil gets completed before the start of the upstroke in the subsequent cycle due to high reduced frequency of the pitching cycle.

5. Recommendations and Future Work

Dynamic stall simulation has been performed on NACA0012 airfoil at two different Reynolds numbers and pitch rates using wall resolved LES. The conclusion from these two studies is that the predicted lift coefficient does not closely match with that of experimental values during downstroke. One of the possible ways of improving the predictions of the aerodynamic coefficients of the flow during the dynamic stall is to either increase the accuracy of spatial discretization scheme of convective terms or to increase the grid resolution with the present numerical scheme. For simulating the dynamic stall at higher Reynolds numbers, the latter option poses severe grid size requirements and is practically infeasible. Therefore there is a motivation to incorporate higher order discretization schemes for better prediction of dynamic stall at practical Reynolds numbers which are typically in the order of few million.

Wall resolved Large Eddy Simulations (LES) of wall-bounded flows at high Reynolds numbers necessitates an extremely fine mesh resolution in the wall proximal inner layer and thus demands huge computational resources and stringent time step requirements. Use of wall modeled LES has been validated for several other applications where a two-layer wall model is used to model the near wall turbulence in the inner wall layer. Recent studies conclude that the formation of Laminar Separation Bubble (LSB) is responsible for the initiation of the Leading Edge Vortex (LEV) which in turn is highly dependent on the prediction and propagation of transition along the pitching airfoil. [40, 41, 51] The next logical step after this study is to incorporate wall modeled LES and transition modeling to analyze the prediction capability of the dynamic stall phenomenon and compare the results with those of wall resolved LES and experimental values.

References

[1] Carr, L. W., 1988, "Progress in Analysis and Prediction of Dynamic Stall," Journal of Aircraft, 25(1), pp. 6-17.

[2] Wernert, P., Geissler, W., Raffel, M., and Kompenhans, J., 1996, "Experimental and Numerical Investigations of Dynamic Stall on a Pitching Airfoil," AIAA Journal, 34(5), pp. 982-989.

[3] McCroskey, W., Carr, L., and McAlister, K., 1976, "Dynamic Stall Experiments on Oscillating Airfoils," AIAA Journal, 14(1), pp. 57-63.

[4] McAlister, K., Carr, L., McCroskey, W., 1978, "Dynamic Stall Experiments on the NACA0012 Airfoil," NASA.

[5] McCroskey, W., McAlister, K. W., Carr, L., and Pucci, S., 1982, "An Experimental Study of Dynamic Stall on Advanced Airfoil Sections. Volume 1. Summary of the Experiment," DTIC Document.

[6] McAlister, K., Pucci, S., McCroskey, W., and Carr, L., 1982, "An Experimental Study of Dynamic Stall on Advanced Airfoil Sections. Volume 2. Pressure and Force Data," DTIC Document.

[7] Leishman, J., 1990, "Dynamic Stall Experiments on the NACA 23012 Aerofoil," Experiments in Fluids, 9(1-2), pp. 49-58.

[8] Schreck, S. J., and Hellin, H. E., 1994, "Unsteady Vortex Dynamics and Surface Pressure Topologies on a Finite Pitching Wing," Journal of Aircraft, 31(4), pp. 899-907.

[9] Raffel, M., Kompenhans, J., and Wernert, P., 1995, "Investigation of the Unsteady Flow Velocity Field Above an Airfoil Pitching Under Deep Dynamic Stall Conditions," Experiments in Fluids, 19(2), pp. 103-111.

[10] Lee, T., and Gerontakos, P., 2004, "Investigation of Flow Over an Oscillating Airfoil," Journal of Fluid Mechanics, 512, pp. 313-341.

[11] Choudhuri, P. G., and Knight, D., 1996, "Effects of Compressibility, Pitch Rate, and Reynolds Number on Unsteady Incipient Leading Edge Boundary Layer Separation Over a Pitching Airfoil," Journal of Fluid Mechanics, 308, pp. 195-218.

[12] Ekaterinaris, J. A., Platzer, M. F., 1997, "Computational Prediction of Airfoil Dynamic Stall," Progress in Aerospace Sciences, 33, pp. 759-846.

[13] Geissler, W., Chandrasekhara, M., Platzer, M., and Carr, L., "The Effect of Transition Modelling on the Prediction of Compressible Deep Dynamic Stall," Proc. 7th Asian Congress of Fluid Mechanics.

[14] Squires, K. D., 2004, "Detached-Eddy Simulation: Current Status and Perspectives," Direct and Large-Eddy Simulation V, R. Friedrich, Geurts, B. J., Métais, O., ed., Springer Netherlands, pp. 465-480.

[15] Sagaut, P., 2006, Large Eddy Simulation for Incompressible Flows, Springer.

[16] Wu, J., Sankar, L., Huff, D., 1989, "Evaluation of Three Turbulence Models for Prediction of Steady and Unsteady Airloads," 27th Aerospace Sciences Meeting, AIAA, Reno, NV.

[17] Srinivasan, G. R., Ekaterinaris, J. A., McCroskey, W. J., 1995, "Evaluation of Turbulence Models for Unsteady Flows of an Oscillating Airfoil," Computers and Fluids, 24(7), pp. 833-861.

[18] Barakos, G. N., Drikakis, D., 2003, "Computational Study of Unsteady Turbulent Flows around Oscillating and Ramping Airfoils," Numerical Methods in Fluids, 42(2), pp. 163-186.

[19] Spentzos, A., Barakos, G., Badcock, K., Richards, B., Wernert, P., Schreck, S., Raffel, M., 2005, "Investigation of Three-Dimensional Dynamic Stall Using Computational Fluid Dynamics," AIAA Journal, 43(5), pp. 1023-1033.

[20] Niu, Y. Y., 1999, "Evaluation of Renormalization Group Turbulence Models for Dynamic Stall Simulation," AIAA Journal, 37(6), pp. 770-771.

[21] Wu, J.-C., Huff, D. L., and Sankar, L., 1990, "Evaluation of Three Turbulence Models in Static Air Loads and Dynamic Stall Predictions," Journal of Aircraft, 27(4), pp. 382-384.

[22] Dindar, M., KAYNAK, U., and FUJII, K., 1993, "Nonequilibrium Turbulence Modeling Study on Light Dynamic Stall of a NACA0012 Airfoil," Journal of Aircraft, 30(3), pp. 304-308.

[23] Rizzetta, D. P., and Visbalt, M. R., 1993, "Comparative Numerical Study of Two Turbulence Models for Airfoil Static and Dynamic Stall," AIAA Journal, 31(4), pp. 784-786.

[24] Rumsey, C. L., and Vatsa, V. N., 1993, "A Comparison of the Predictive Capabilities of Several Turbulence Models using Upwind and Central-Difference Computer Codes," AIAA Paper(93-192).

[25] Sheng, W., Galbraith, R. M., and Coton, F., 2008, "A Modified Dynamic Stall Model for Low Mach Numbers," Journal of Solar Energy Engineering, 130(3), p. 31013.

[26] Mehta, U. B., 1978, "Dynamic Stall of an Oscillating Airfoil," AGARD Unsteady Aerodyn, pp. 1-32.

[27] Ghia, K., Yang, J., Osswald, G., and Ghia, U., 1991, "Study of the Dynamic Stall Mechanism Using Simulation of Two-Dimensional Navier-Stokes Equations," AIAA Paper(91-0546), pp. 7-10.

[28] Tuncer, I., Wu, J., Wang, C., 1990, "Theoretical and Numerical Studies of Oscillating Airfoils," AIAA Journal, 28(9), pp. 1615-1624.

[29] Wu, J., 1984, "Fundamental Solutions and Numerical Methods for Flow Problems," International Journal for numerical methods in fluids, 4(2), pp. 185-201.

[30] Wu, J., 1981, "Theory for Aerodynamic Force and Moment in Viscous Flows," AIAA Journal, 19(4), pp. 432-441.

[31] Sankar, N., and Tassat, Y., 1981, "Compressibility Effects on Dynamic Stall of an NACA 0012 Airfoil," AIAA Journal, 19(5), pp. 557-558.

[32] Sankar, N., and Tassa, Y., 1980, "Reynolds number and Compressibility Effects on Dynamic Stall of a NACA 0012 Airfoil," AIAA, 18th Aerospace Sciences MeetingPasadena, CA.

[33] Rumsey, C. L., and Anderson, W. K., 1988, "Some Numerical and Physical Aspects of Unsteady Navier-Stokes Computations Over Airfoils Using Dynamic Meshes," AIAA, 26th Aerospace Sciences MeetingReno, NV.

[34] Ekaterinaris, J., 1989, "Compressible Studies on Dynamic Stall," AIAA 27th Aerospace Sciences MeetingReno, NV.

[35] Wang, S., Ingham, D. B., Ma, L., Pourkashanian, M., Tao, Z., 2010, "Numerical Investigations on Dynamic Stall of Low Reynolds Number Flow Around Airfoils," Computers and Fluids, 39, pp. 1529-1541.

[36] Leishman, J. G., 2006, Principles of Helicopter Aerodynamics, Cambridge University Press.

[37] Martinat, G., Braza, M., Hoarau, Y., Harran, G., 2008, "Turbulence Modeling of the Flow Past a Pitching NACA0012 airfoil at 10^5 and 10^6 Reynolds Numbers," Journal of Fluids and Structures, 24, pp. 1294-1303.

[38] Fung, K.-Y., and Carr, L., 1991, "Effects of Compressibility on Dynamic Stall," AIAA journal, 29(2), pp. 306-308.

[39] Currier, J. M., and Fung, K.-Y., 1992, "Analysis of the Onset of Dynamic Stall," AIAA journal, 30(10), pp. 2469-2477.

[40] Visbal, M. R., "Analysis of the Onset of Dynamic Stall Using High-Fidelity Large-Eddy Simulations," Proc. AIAA SciTech 52nd Aerospace Sciences Meeting

[41] Visbal, M. R., 2009, "High-Fidelity Simulation of Transitional Flows Past a Plunging Airfoil," AIAA Journal, 47(11), pp. 2685-2697.

[42] Germano, M., Piomelli, U., Moin, P., and Cabot, W. H., 1991, "A dynamic subgrid-scale eddy viscosity model," Physics of Fluids A, 3, pp. 1760-1765.

[43] Tafti, D. K., 2001, "GenIDLEST: A Scalable Parallel Computational Tool for Simulating Complex Turbulent Flows," ASME-PUBLICATIONS-FED, 256, pp. 347-356.

[44] Tsai, H., F. Wong, A., Cai, J., Zhu, Y., and Liu, F., 2001, "Unsteady Flow Calculations With a Parallel Multiblock Moving Mesh Algorithm," AIAA Journal, 39(6), pp. 1021-1029.

[45] Dubuc, L., Cantariti, F., Woodgate, M., Gribben, B., Badcock, K., and Richards, B., 2000, "A Grid Deformation Technique for Unsteady Flow Computations," International Journal for Numerical Methods in Fluids, 32(3), pp. 285-311.

[46] Sadeghi, M., and Liu, F., "Coupled Fluid-Structure Simulation for Turbomachinery Blade Rows," Proc. 43rd AIAA Aerospace Sciences Meeting and Exhibit, pp. 2005-0018.

[47] Gopalakrishnan, P., and Tafti, D. K., 2009, "A Parallel Boundary Fitted Dynamic Mesh Solver for Applications to Flapping Flight," Computers & Fluids, 38(8), pp. 1592-1607.

[48] Jovičić, N., and Breuer, M., 2005, "High-Performance Computing in Turbulence Research: Separated Flow Past an Airfoil at High Angle of Attack," High Performance Computing in Science and Engineering, Munich 2004, Springer, pp. 93-105.

[49] Berton, E., Allain, C., Favier, D., Maresca, C., 2002, "Experimental Methods for Subsonic Flow Measurements," Notes on Numerical Fluid Mechanics and Multidisciplinary Design (dedicated volume in Progress in Computational Flow-Structure Interaction), W. Haase, Selmin, V., Winzell, B., ed., Springer, pp. 251-260.

[50] Tafti, D., 1996, "Comparison of Some Upwind-Biased High-Order Formulations with a Second-Order Central-Difference Scheme for Time Integration of the Incompressible Navier-Stokes Equations," Computers & fluids, 25(7), pp. 647-665.

[51] Medida, S., and Baeder, J. D., "Numerical Investigation of 3-D Dynamic Stall using Delayed Detached Eddy Simulation," Proc. 50th AIAA Aerospace Sciences Meeting including the New Horizons Forum and Aerospace Exposition.

Appendix – Coherent Structures Formation

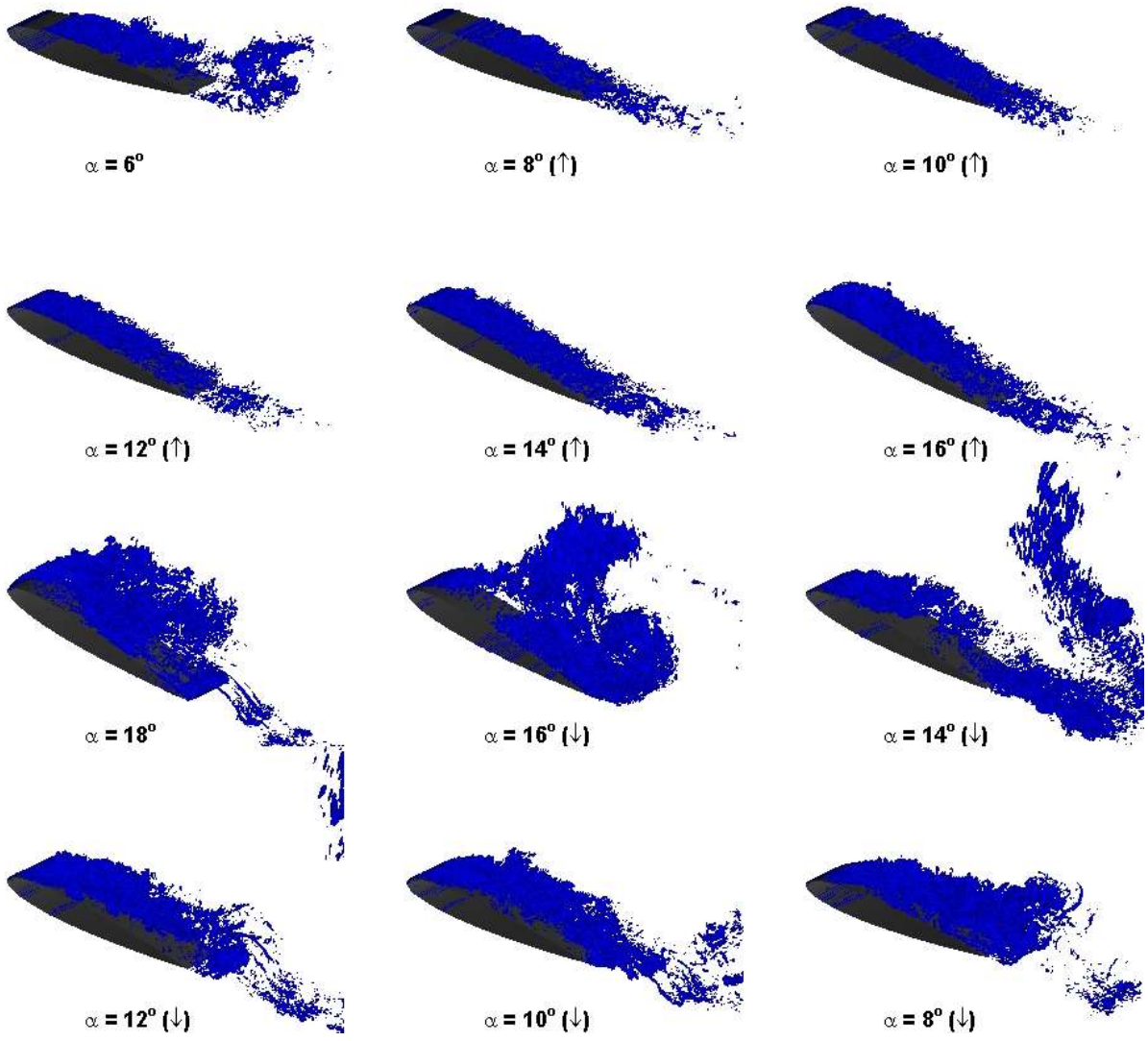

Figure A. 1: Coherent Structures Formation during the Dynamic Stall at Re = 10^5 and k = 0.188

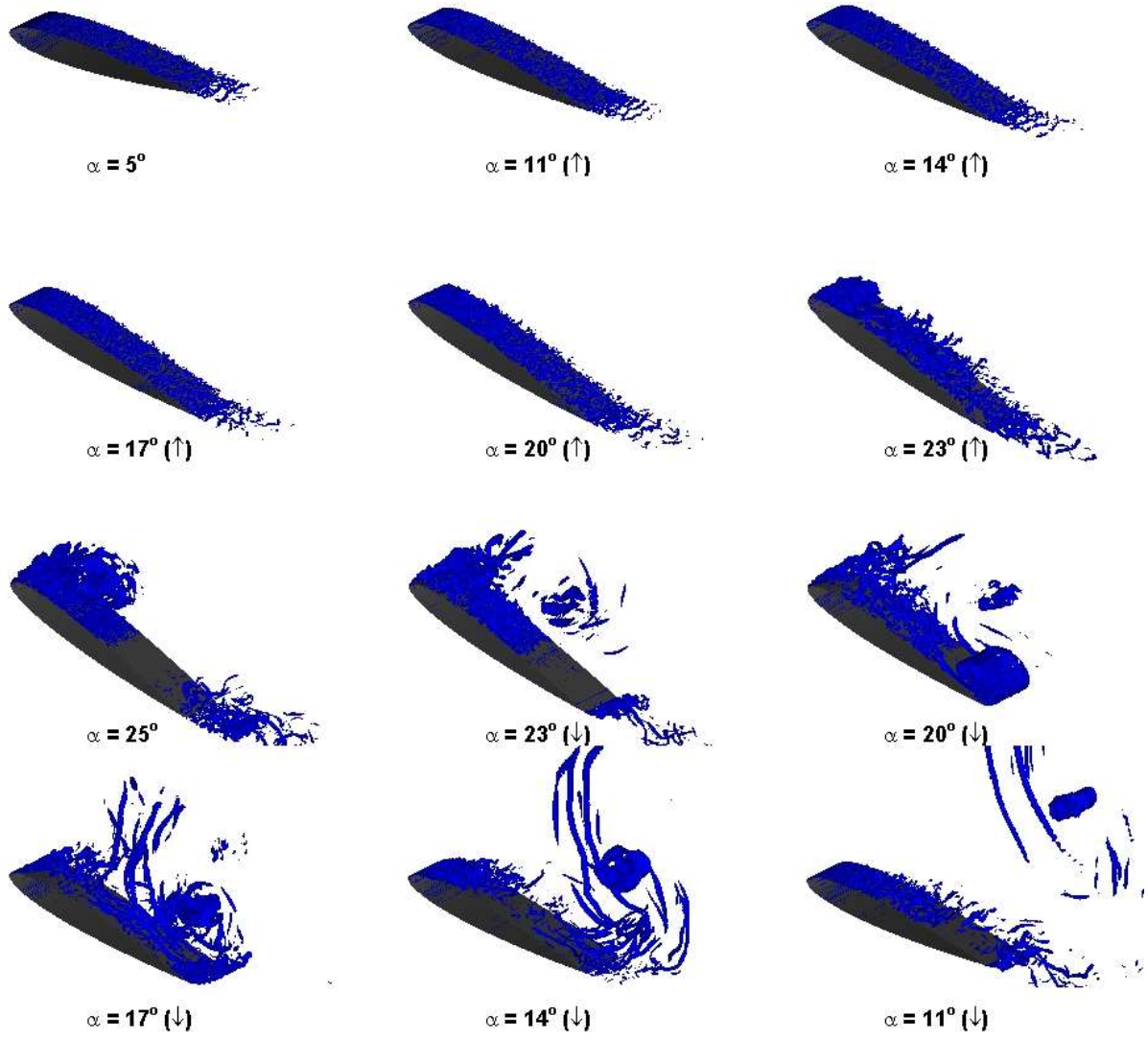

Figure A. 2: Coherent Structures Formation during the Dynamic Stall at Re = 10^6 and k = 0.25